A Coherent Diffractive Imaging Facility at NSLS-II
Conceptual Design Report

May 9, 2019

Contents

List of Figures **3**

List of Tables **4**

1 Introduction **5**
- 1.1 Background . . . 5
- 1.2 Executive summary . . . 5
- 1.3 Science targets . . . 6
  - 1.3.1 Semiconductors . . . 7
  - 1.3.2 Complex Oxides . . . 7
  - 1.3.3 Alternative Catalysts . . . 7
  - 1.3.4 Nanoscale Mechanical Materials . . . 8
  - 1.3.5 Energy Conversion Materials . . . 8
- 1.4 Document Structure . . . 8
- 1.5 Contributors . . . 9

2 Optical Design **10**
- 2.1 Front-end Design . . . 11
  - 2.1.1 Undulator . . . 12
  - 2.1.2 X-ray beam position monitor . . . 13
- 2.2 Optical Simulations . . . 14
- 2.3 60-m optical scheme . . . 15
- 2.4 100-m optical scheme . . . 16
- 2.5 Comparison of optical designs . . . 16
- 2.6 Comparison of floor plans . . . 21
- 2.7 Fundamental harmonic filter . . . 23
- 2.8 Slits . . . 25
- 2.9 Monochromators . . . 25
  - 2.9.1 Double crystal monochromator . . . 25
  - 2.9.2 Horizontal vs vertical deflection . . . 27
  - 2.9.3 Multilayers . . . 28
  - 2.9.4 Monochromator offset . . . 29
  - 2.9.5 Finite element analysis of filter, DCM, and DMM . . . 29
- 2.10 Mirrors . . . 30
  - 2.10.1 Pre-focusing optics . . . 30
  - 2.10.2 Final focusing optics . . . 30
  - 2.10.3 Incidence angles . . . 31
  - 2.10.4 Motion of optics . . . 32
  - 2.10.5 Visualization . . . 32
  - 2.10.6 Feedback . . . 32

2.11 Exit window . . . 33

3 Endstation Design **33**
3.1 X-ray transport . . . 34
3.2 Sample positioning . . . 34
3.2.1 Goniometer . . . 34
3.2.2 Scanning stages . . . 35
3.3 Environmental requirements . . . 35
3.4 Detection . . . 36
3.4.1 Detector technology . . . 38
3.4.2 Detector Positioning . . . 39
3.5 Time-resolved provisioning . . . 40

4 Controls Considerations **40**

5 Preliminary Comments on a Satellite Building **40**

6 Safety **42**

References **46**

List of Figures

1 Performance of light sources. 5
2 The CDI beamline concept. 6
3 Novel CDI geometries. 7
4 The beamline layout. 10
5 The NSLS-II front end. 12
6 Spectral brightness of possible undulators. 13
7 Spectral brightness of room-temperature, in vacuum undulators. 14
8 Simulation of fully coherent intensity and phase 15
9 Cuts through simulated coherent intensity and phase 16
10 Simulation of the intensity and coherence of a 1 micron spot in the short concept. 17
11 Simulation of the intensity and coherence of a 10 micron spot in the short concept. 18
12 Simulation of the intensity and coherence of a 1 micron spot in the long concept. 19
13 Simulation of the intensity and coherence of a 10 micron spot in the long concept. 20
14 A table of the parameters for the two optical designs. 21
15 A layout at 29-ID. 22
16 A layout in a satellite building. 23
17 Transmission through the harmonic filter. 25
18 The dual monochromator scheme. 27
19 DCM and DMM modes of operation. 27
20 Relative reflectivity of a horizontal DCM. 27
21 The Power Density Distribution after the CDI Filter. 29
22 DMM 1st Multilayer Mirror Cooling Scheme 30
23 DMM temperature, displacement, and stress distributions 31
24 The 1st multilayer mirror surface profile thermal performance. 31
25 DCM 1st crystal thermal performance. 32
27 Feedback results from HXN. 32
26 Total reflectivity of the proposed mirror system. 33
28 Sample working space. 34
29 RMS displacement of the floor at 29-ID. 36
30 RMS displacement of the floor at HXN. 37
31 Comparison of the performance at 29-ID and HXN. 38
32 Detector motion system concept. 40
33 Proposed satellite building properties. 41

List of Tables

1 A comparison of the long and short options. 24
2 Specifications for DMM motions. 26
3 Specifications for DCM motions. 26
4 The 1st multilayer mirror surface slope errors. 29
5 Maximum full-field sample size for modes of operation 39

1 Introduction

This report contains the conceptual design for a new beamline, proposed at NSLS-II, to measure the structure, deformation, and fast dynamics in materials systems. Performing these measurements on real-world functional materials will enable knowledge-directed materials engineering. In a full-field mode, the beamline will use 5-15 keV x-ray photons to probe polycrystalline samples up to 10 µm in size at nanoscale resolution. By scanning the sample through the x-ray beam, much larger samples can be examined with the same resolution. The combination of this instrument with the highly coherent source at NSLS-II will result in a powerful tool for the study of materials systems.

1.1 Background

X-ray coherent diffractive imaging (CDI) has been developed as a non-invasive, lens-less technique to probe material structure on the nanoscale. Forward-scattering CDI can be used to produce a 3D image of micron-sized or larger samples, with nanometer-scale resolution, from measurements of the transmitted x-ray intensity. 3D images are vital to understanding the interrelationship between between nanoscale local phenomena and the behavior of the entire system. These images, with suitable prior knowledge, can provide information regarding density or elemental composition with nanoscopic resolution. The density and composition information can provide invaluable information about transport of material within a sample and the relationship between structure and function. Bragg CDI utilizes the same procedure; however, the data are collected at Bragg reflections. This allows a Bragg CDI measurement to determine a 3D map of the deformation field inside a crystal, with very high sensitivity, simultaneous to the determination of its shape[1, 2, 3, 4, 5, 6, 7, 8, 9]. The third spatial dimension is provided by combining many 2D patterns measured either at each point along a rocking curve scan of the crystal reflection or during a scan of the incident energy, far from any atomic or molecular resonance, which effectively scans along the radial direction through a reflection in the Ewald construction.

Understanding the deformation of a material from its ideal lattice is vital to the prediction of a material's function, aging, and failure. These techniques were foreshadowed by Sayre[10] in 1952, demonstrated by Miao[11] in 1999, and are routinely applied to a wide range of materials at recent-generation, storage-ring-based x-ray facilities[12, 13].

NSLS-II is a state-of-the-art third generation storage ring facility, providing an electron beam with high emittance. These properties are the basis for a highly desirable coherent x-ray source for use in CDI. A snapshot of current and future storage-ring source properties is shown in Fig. 1.

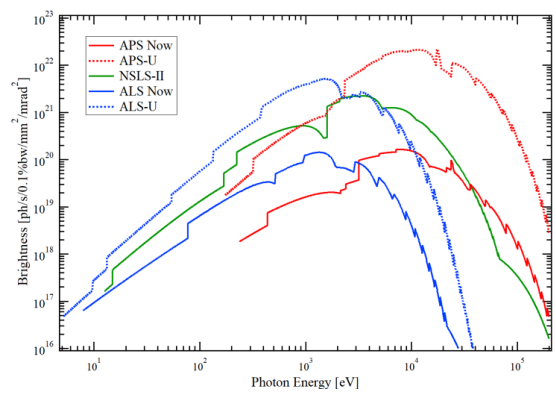

Figure 1: Current performance and upgraded spectral brightness envelopes, containing all insertion devices, for selected operating US storage-ring-based light sources. The NSLS-II brightness envelope was calculated at the assumption 0.8 nm horizontal emittance and 500 mA current of the electron beam.

1.2 Executive summary

The requirements on the x-ray illumination to make these nanoscale resolution measurements are high: the traditional method calls for complete transverse and longitudinal coherence, while recent work[14, 15] reveals modifications that substitute an understanding of the beam, within known limits. The proposed beamline will use a four-mirror focusing system to provide a spot size of up to about 10 microns in diameter and down to below 1 micron at the sample location, which is coincident with the waist of the x-ray beam. This system will allow the total flux to remain essentially the same for each x-ray spot in this range. The optical design allows for achromatic focusing, which permits the exploitation of anomalous scattering and the scanning of photon energy. The transverse, i.e., spatial, coherence length of the beam

will be tunable and the longitudinal coherence will be set by a monochromator. Two crystal pairs will be used: Si(111) crystals will be employed for routine work on micron-sized samples; and a Si(311) pair will be available for the largest samples and those requiring a large scattering angle. A double multilayer monochromator will also be available and used for locating crystalline grains within a sample and to provide additional partially-coherent flux to samples that require this, for example, nm-sized crystalline grains.

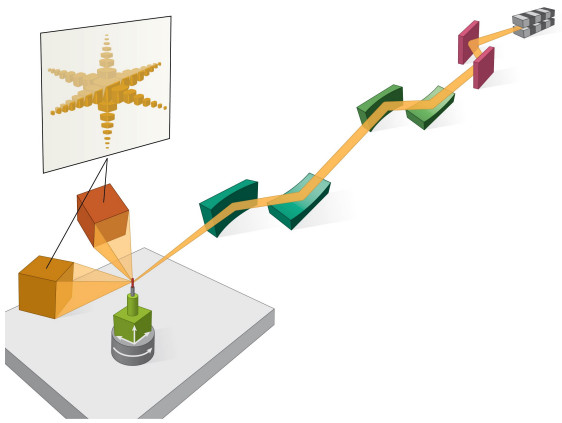

Figure 2: A schematic demonstrating the CDI beamline concept. A four-mirror focusing system provides a "zoomable" spot size and coherent scattering data is measured in two independent detectors. The optical system is essentially achromatic and the coherence properties of the beam can be controlled.

To address the challenge of robustly and flexibly imaging ordered and amorphous materials with typical sizes in the micron range at nanoscale resolution, CDI is a natural choice of technique. The efficient design of such an instrument requires an understanding of the impact of the x-ray detector and the measurement geometry. In CDI, continuous diffraction patterns are measured in 2D, while 3D information is collected by scanning the "pose"—the position and orientation—of the sample or the incident photon energy. To a first approximation, the extent of the measured diffraction pattern—the angle subtended by the detector—determines the best possible resolution of the resulting image, while the sampling period—typically the pixel pitch—determines the field of view. These considerations allow the specification of a detection system, given the targeted sample and feature size and the instrument photon energy range.

The requirement for imaging single crystals of several microns in size at nanoscale resolution—over the photon energy range from 5 to 15 keV, where NSLS-II provides an exceptionally high-brightness source—with currently available x-ray detectors is that the maximum reasonable sample-to-detector distance is of order 8 m, with a minimum displacement of about 0.5 m. To support simultaneous measurement of multiple-Bragg-reflection, forward- and Bragg-scattering, and multiple-grain Bragg-scattering CDI, two detectors should independently positionable in a large region of reciprocal space. This capability is a unique feature of the design that will provide complementary information that is not currently available at any coherence imaging instrument. The deformation sensitivity of the method scales with the order of the Bragg reflection, instituting a requirement for large-angle scattering measurements. These geometries are sketched in Fig. 3.

The sample will be positioned on a flexible goniometer that will allow a reasonable loading to accommodate environmental cells. These cells might provide for gas or liquid flow, contain high pressure environments, or be cryogenically cooled. A fast-scanning axis will be provided to support methods like ptychography. The working distance of the optics will be approximately 0.5 m, allowing for unusual cell geometries, ancillary detectors to monitor the beam or sample, or the implementation of probe devices, such as a magnetic or laser optical system.

1.3 Science targets

Increasingly, advanced functional materials are heterogeneous. The behavior of polycrystals, materials composed of multiple highly-ordered regions or crystal grains, often depend upon the intergrain interactions, which could be elucidated through Bragg CDI investigations of multiple individual grains with the polycrystal. Some materials of interest can also exhibit a very low degree of long-range order, being primarily amorphous with small crystalline regions. In these cases, 3D images of the structure and deformation of the ordered regions from Bragg CDI might be combined with 2D images, derived from forward-scattering CDI, to form a more complete picture of the interplay between amorphous and crystalline regions with the sample. Samples of real materials also tend to display heterogeneity over several decades of length-scale. A strength of CDI is that, at hard x-ray energies provided by at NSLS-II, it can conveniently be used to image

several-micron-sized particles at nanoscale resolution. The following describes several example research areas that would benefit from a state-of-the-art x-ray CDI beamline.

1.3.1 Semiconductors

Strain is important for mobility and band gap engineering techniques used in the present generation of CMOS devices and in the emerging world of silicon quantum electronics. Bragg CDI has been used by Thomas et al. [16] to examine individual strained Silicon-on- Insulator (SOI) structures. Strain patterns can be created in model devices with sizes more relevant to current technology (22nm), that penetrate partially into the thickness of the SOI layer, as is relevant. As Thomas et al. found, Bragg CDI is particularly valuable in devices fabricated using SOI because the active layer of Si has a different orientation from the much thicker handle[16]. The challenge of manipulating the structure of silicon includes creating interfaces with graphene and other emerging two-dimensional electronic materials and integrating other functionalities into silicon electronics. Bragg CDI studies of nanowire structures have come out of ID01 at ESRF, which has become a major center for this activity [17]. The laser-excitation of nanowire structures is a large untapped area for pump-probe Bragg CDI. It is even possible to image lattice distortions in semiconductor heterostructures[9].

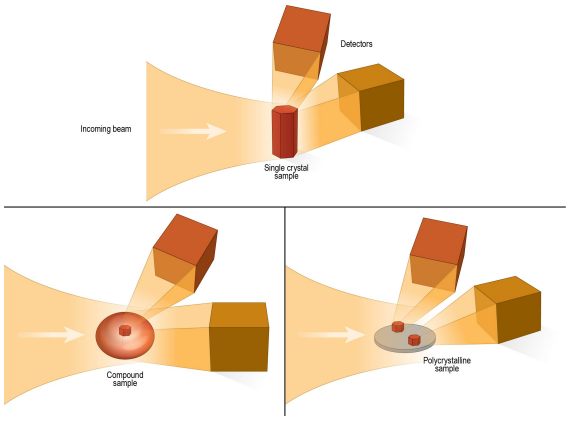

Figure 3: Three of the novel scattering geometries supported by the proposed instrument: (Top) the simultaneous measurement of two Bragg peaks from the same crystal; (Bottom-left) the simultaneous measurement of an amorphous sample in 2D and a crystal in within it in 3D; and (Bottom-right) the simultaneous measurement of two grains within a large polycrystal.

We plan to interact with the user community to develop UHV growth chambers compatible with Bragg CDI beamline. These will be used both for in-situ growth studies of nanowires and other nanocrystals as well as their laser excitation. Special consideration will be required for the design of a common X-ray/laser window system. There is significant user interest in time resolved Bragg CDI of polycrystalline films both in the GISAXS geometry[18] and in the Bragg-angle domain. Even under steady state growth there are strong density fluctuations in sputtered films that couple with the surface roughness to give a heterodyne coherent interference signal, which can reveal detailed structural information about both the film 'bulk' and the growing surface[18].

1.3.2 Complex Oxides

These materials can be driven far from equilibrium by external electric fields. X-ray scattering techniques couple directly to the order parameters relevant to ferroelectricity and magnetism, providing results that are fully quantitative [19]. Bragg CDI can resolve small strains with spatial resolution far better than selected-area diffraction approaches. In addition, coherent scattering experiments can have time-resolutions limited only by the bunch length of the pulses from the storage ring, which will be on the order of 30 ps at NSLS-II. Phenomena accessible with the dramatic advance in spatial and temporal resolution include domain dynamics, the physics of magnetoelectric coupling, the coupling of soft modes to applied fields, coupling of strain between components of multilayers and multicomponent multifunctional materials.

1.3.3 Alternative Catalysts

Zeolite and perovskite oxide materials have both been proposed as alternatives to Platinum-Group Metal (PGM) automotive emission catalysts, with the advantage of being substantially cheaper [20]. Perovskites are classical mixed-ion oxides with composition ABO_3. The oxygen coordination is cuboctahedral (12-fold) around the A site and octahedral around B. The discovery in 2010 that $La_{(1-x)}Sr_xMnO_3$ (LSMO) and

$La_{(1-x)}Sr_xCoO_3$ (LSCO) perovskites were as effective as PGMs for removing NO_x from diesel exhaust was an important breakthrough[21]; this class of oxides had been found ineffective before and thought to become active catalysts by virtue of having Sr++ active sites. Zeolites are crystalline Aluminosilicate composites with a regular nano-porous lattice structure which allows gases to reach active sites within their framework. The zeolites most relevant to automotive catalysts are ZSM-5 and SAPO-34. We will provide gas handling sample environments for operando experiments to observe the strains within these micro-crystalline oxide catalysts while they perform their reactions. Bragg CDI can obtain 3D images of distortions of the internal "plumbing" of the nano-porous network which provides their large surface area and selectivity during reactions. The expected resolution, in the nanometer range, is insufficient to see the 0.5 nm pores directly, but the strain sensitivity is much better than a lattice constant; crystal distortions in the picometre range can be detected when they extend over the resolution range. The nanometer length scale is well-matched to the expected scale of distortions due to "coking" which results in catalyst lifetimes too short for commercial exploitation. A potentially new area of laser-promoted ultrafast catalysis can be explored using time domain Bragg CDI experiments.

1.3.4 Nanoscale Mechanical Materials

Mechanical deformation is vital to the operation and development of state-of-the-art devices in sensing, data storage, and optomechanics, as well as the engineering of ultrastrength materials. By measuring the force required to fracture micron-sized single crystal diamond, needles [22] have been shown to exhibit ultralarge elastic deformation. Using Bragg CDI, such experiments would recover the nanoscale deformation, providing additional input to the modeling of such systems. This allows for enhanced materials engineering with feedback on materials performance provided with nanoscale resolution. In the case of polycrystalline materials, the method could allow the simultaneous mapping of deformation within neighboring grains in a micron-sized feature. In quantum information science, the nitrogen vacancy within diamond resonators is among the most promising implementations of a qubit. Attempts are on-going[23] to fully characterize the strain dependency of the vacancy ground state. With Bragg CDI, the data from each reflection results in deformation projected along one momentum transfer vector. The measurement of multiple reflections simultaneously is an efficient way to recover the full strain tensor of a crystal. In these potential qubit systems, the deformation mapping and sensitivity of Bragg CDI, coupled with the ability to measure structural evolution, could add invaluable insight to the materials science underlying quantum information science.

1.3.5 Energy Conversion Materials

Thermoelectric materials may be a future replacement for traditional compressor-based cooling and refrigeration devices. Since these directly convert between heat and electricity, their further development may also lead to waste-heat recovery technologies. The primary loss mechanism is through sustained phonon modes, which increase the thermal conductivity, within the crystalline domains of the device. Recently, it was demonstrated that record-setting performance of a Bi_2Te_3 material could be achieved by creating a composite material of micron-sized grains with nanoscale crystalline inclusions[24]. With Bragg CDI, it will be possible to image few-micron sized crystals with sufficient spatial resolution to resolve the nanoscale features. The deformation information gained near the boundaries may lead to even more effective strategies for phonon scattering and thereby to more efficient thermoelectric devices. The high coherent flux and variable x-ray spot size provided by a Bragg CDI instrument will enable in operando experiments on this system and many others. Sections 4 to 6 provide supporting information on controls, construction, and safety.

1.4 Document Structure

In the remainder of this document, we present our plans to deliver a tool to advance the understanding of materials systems, including those described above. In Section 2, we present our preferred achromatic, 100-m-long optical system that will provide a continuously zoomable spot size in the 1 to 10 micron range without loss of x-ray flux. A novel feature of the optical design is the ability to vary the coherence properties of the incident beam, for example, to provide as many x-rays as possible to a evolving sample or a nearly perfect beam to a sample with subtle lattice distortion. That spot will be delivered to an endstation, whose concept is described in Section 3. A clear area surrounding the sample will be preserved for the introduce

of new sample environmental cells. A goniometer with scanning capability will be proposed to support the application of the method to a wide range of samples. Finally, the detector motion system needs and a proposed concept will be presented to deliver on our novel capability to perform several simultaneous coherent imaging experiments.

1.5 Contributors

The CDI beamline project team consists of G. Williams, scientific lead, L. Berman, project manager, Yi Zhu, project engineer, O. Chubar, optics and source simulation scientist, and M. Idir, x-ray optics scientist, with assistance from S. Hulbert and Y. Chu. C. Spataro and F. Lincoln have conducted numerous measurements of facility vibrational stability.

The CDI beamline advisory team is comprised of I. Robinson, R. Harder, A. Mancuso, R. Sandberg, and O. Sphyrko. Robinson and Mancuso have directly contributed to this report.

2 Optical Design

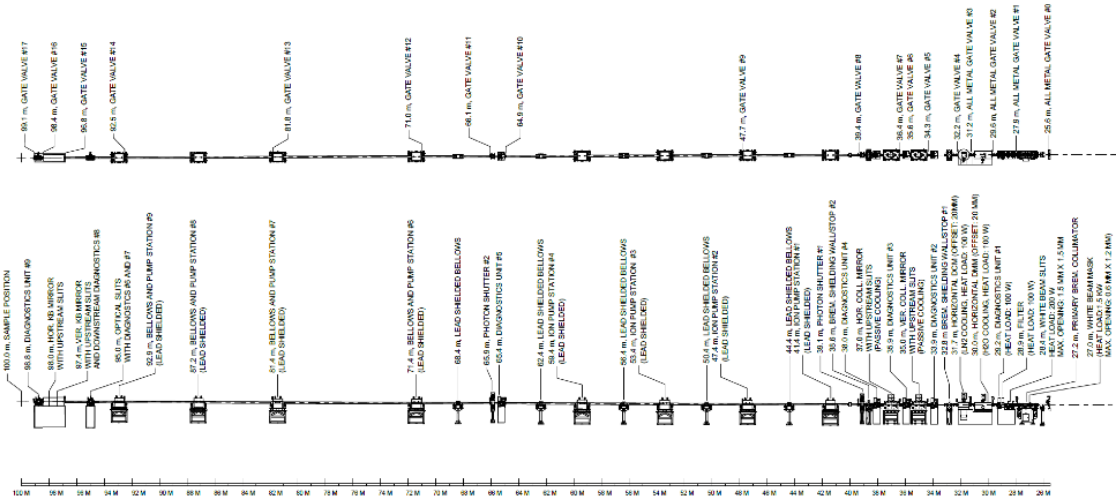

Figure 4: The full layout of the proposed beamline. Individual components and their locations are called out in the text.

To address the science cases described above and optimize a Bragg coherent diffractive imaging instrument for NSLS-II, we set the following design goals for our optical system:

1. To maximize impact from the source, the coherence of the illuminating field should be variable. The design target is to provide coherence lengths in the illumination that vary from much-longer-than to around 20% of the respective dimension of the sample.

2. The transverse x-ray spot size should be variable from around 10 µm to less than 1 µm in diameter without moving the interaction point between the x-rays and the sample.

3. The interaction point should be independent of the photon energy in the illuminating field.

4. The field near the interaction plane should be as free from aberration, phase error, and instability as is possible.

5. The working distance of the final optics should be long.

Points 1 and 2 support the ideal of providing as many usable x-rays to the interaction point as is possible. This capability drives time-resolved studies and, more practically, can reduce the long-term stability requirements of the remainder of the instrument. The requirement of point 3, an achromatic optical system, is driven by the need to support x-ray resonance contrast imaging and the 3D scanning of the diffraction intensity along the energy axis for use in CDI reconstruction. Point 4 highlights the role of the illuminating field in the recovered CDI micrographs, i.e., that an imperfect or poorly understood illumination could give rise to an erroneous interpretation of the resultant images. A state-of-the-art CDI instrument should be designed with an explicit attention paid to its capabilities in supporting in situ and operando science; point 5 supports these capabilities by providing adequate stand-off areas to accommodate sample cells, diagnostics, and novel detection geometries.

A four-mirror optical system has been developed to support the needs identified above. Kimura et al.[25] have previously proposed such a system based on four, two each horizontally- and vertically-deflecting, deformable x-ray mirrors. We have chosen an optically equivalent scheme that is similarly comprised of two pairs of horizontally- and vertically-deflecting, but wherein one pair of mirrors is deformable and the other has fixed-figure. Formally, in this latter scheme, the horizontal and vertical mirrors must move with respect to one another along the optical axis of the system. From upstream to downstream(See Fig. 4.), the proposed beamline components and their distance from the source point are:

27.0 m white beam mask, NSLS-II standard design;

27.2 m primary Bremstrahlung collimator, NSLS-II standard design;

28.4 m white beam slits, NSLS-II standard design;

28.9 m fundamental harmonic filter, CVD diamond filter with 20 µm thickness;

29.2 m diagnostic stand, beam visualization;

30.0 m double multilayer monochromator (DMM), 0.1% bandpass, horizontally deflecting;

31.7 m double crystal monochromator (DCM), Si(111) and Si(311) crystal pairs, horizontally deflecting;

32.8 m Bremstrahlung shielding, to be designed to NSLS-II standards;

33.9 m diagnostic stand, visualization;

35.0 m first vertical mirror, bendable, silicon surface only;

35.9 m diagnostic stand, visualization;

37.0 m first horizontal mirror, bendable, silicon surface only;

38.0 m diagnostic stand, visualization and beam position monitor;

38.6 m Bremstrahlung shielding, to be designed to NSLS-II standards;

39.1 m photon shutter, NSLS-II standard design;

65.4 m diagnostic stand, visualization and beam position monitor;

65.9 m photon shutter, NSLS-II standard design;

95.0 m slits, low scattering;

97.4 m vertical KB mirror, fixed figure mirror, movable along optical axis;

98.0 m slits, well-polished;

98.0 m horizontal KB mirror, fixed figure, movable along optical axis;

98.8 m diagnostics, visualization and beam position monitor; and

100 m sample-x-ray interaction point.

Below, we present design considerations for the x-ray source, front end, and two related optical designs, each providing about 500 mm of clear distance between the sample and the mirror vacuum chamber, discuss their relative merits before describing the details of individual components in the schemes. A schematic layout of the preferred, 100-m-long optical design is show in Fig. 2. Section 3 contains details of the endstation concept.

2.1 Front-end Design

Fig 5 shows the standard NSLS-II front-end components, where an insertion device, not shown, will occupy the space to the right, upstream of the two x-ray beam position monitors (XBPM). The proposed beamline is not expected to require significant modifications to this design.

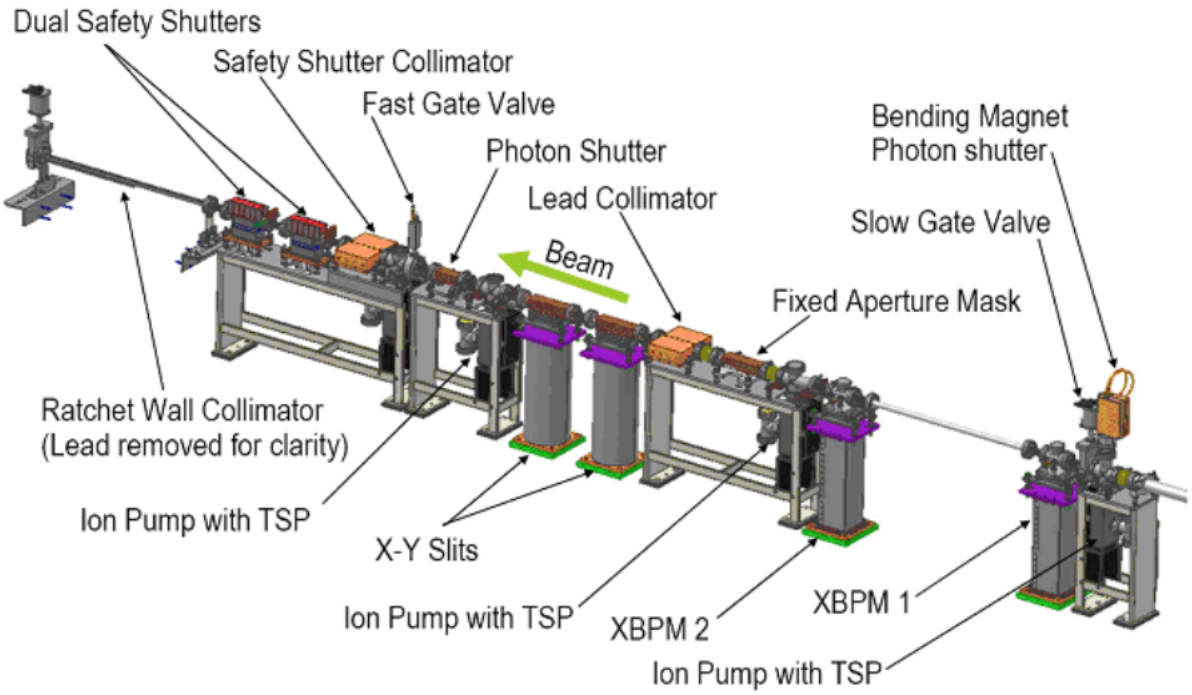

Figure 5: A typical NSLS-II front-end layout. The front-end for the CDI beamline is expected to be nearly identical.

2.1.1 Undulator

The spectral range of the Bragg CDI beamline, spanning 5 - 15 keV, can be easily covered at a 3 GeV storage-ring facility by different types of small-gap small-period undulators, see Figs. 6 and 7. The most conservative option is a commercially available hybrid in-vacuum undulator (IVU) similar to a 3-m long, 5-mm minimum gap, 20 mm period undulator, referred to as IVU20, that is used at NSLS-II beamline, for example, at HXN, the Hard X-ray Nanoprobe. This undulator covers the required spectral range with its undulator radiation (UR) harmonics 3 through 11. Preliminary parametric optimization of a room-temperature IVU option was performed using the magnetostatics code Radia [26] and synchrotron radiation code SRW [27], for currently available comprehensive magnetic materials (Namely, Dy-doped NdFeB with remnant magnetization of 1.19 T for permanent magnets and Va Permendur steel with saturation at ∼2.4 T.) and the electron beam vertical "stay-clear" constraint for the low-beta straight section of NSLS-II, where the beamline undulator source of the beamline will be installed. The results of these calculations, see Fig. 6, suggest that the highest brightness and flux can be provided by IVUs with periods of 18-19 mm, lengths between 2.2-2.9 m and minimum gaps of 4.2-4.9 mm.

Higher spectral brightness and flux, up to factor of 1.5 - 2 at high photon energies, can be offered by a more performant, e.g., superconducting, undulator technology, as shown in Fig. 6. This type of undulator is currently under development at APS / ANL [28]; however, the superconducting undulators (SCU) that were constructed there so far have larger gaps, an approximately 8 mm clear aperture, and shorter lengths, at around 1.5 m, than is required for the best magnetic and spectral performance for the Bragg CDI beamline at NSLS-II (Best performance would require a 4 mm clear aperture, 5.8 mm magnetic gap, 2 m length, and 15.7 mm period.). Nevertheless, there are hopes that by the time of construction of this beamline, the superconducting undulator technology will mature further.

Aside from the room-temperature IVU and SCU, cryo-cooled IVUs–also known as cryo-cooled permanent magnet undulators, CPMUs–could be considered for the Bragg CDI beamline. Spectral performance of such undulators is somewhat inferior to an ideal SCU, see Fig. 7, where CPMU and SCU spectral curves are shown in comparison with those of IVU20. However, this technology has proven to be sufficiently mature for the required parameters as of the time of this writing[29, 30]. Finally, for each of the three magnet technologies–

IVU, CPMU, SCU–a segmented adaptive gap undulator (SAGU) concept could be considered[31]. This would further increase the corresponding undulator spectral performances, as shown by dashed lines in Fig. 7. The decision about the final choice of the type of undulator will be made in near future, taking into account strategies concerning undulator R&D at NSLS-II, potential risks and total budget for the Bragg CDI beamline; however, our **current preference is for a room-temperature in-vacuum undulator with a magnetic period of 18-20 mm**, representing a favorable combination of risk and performance.

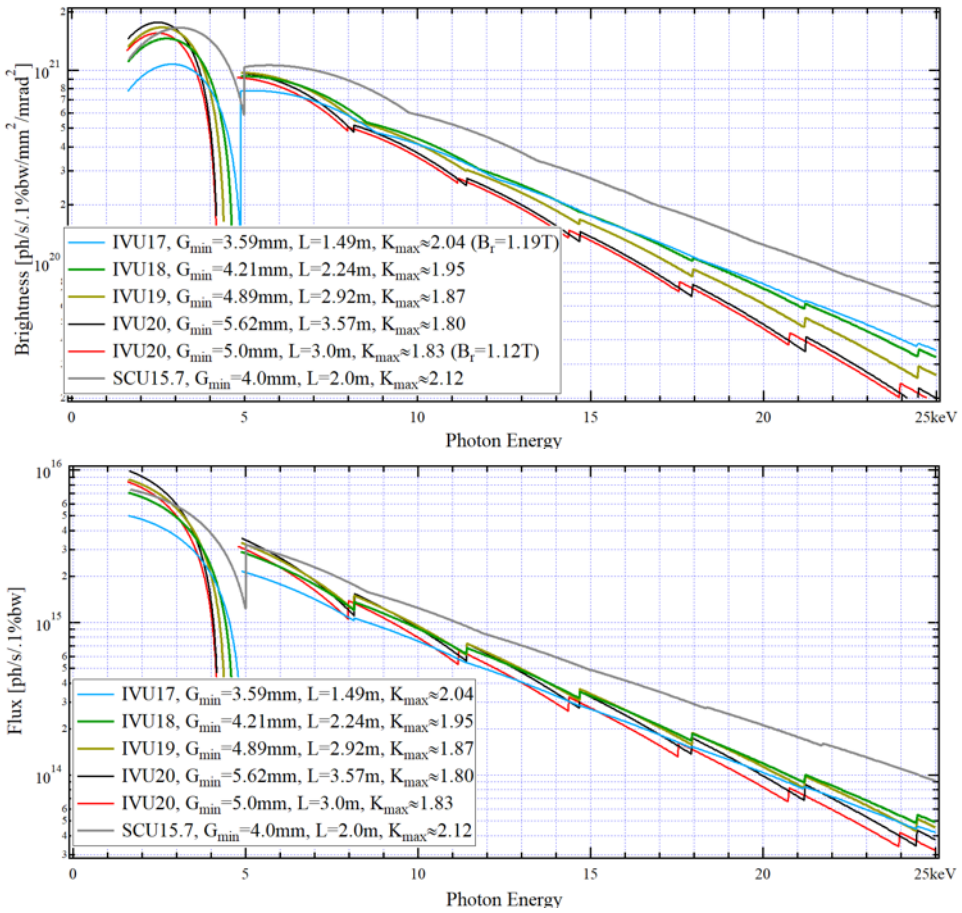

Figure 6: Approximate spectral brightness and flux curves of possible room-temperature in-vacuum undulators with different periods and lengths, all satisfying spectral requirements of the Bragg CDI beamline and the vertical electron beam "stay clear" constraint for the low-beta straight section of NSLS-II. Spectral curves for an optimized (projected) superconducting undulator are also shown, for comparison. The NSLS-II "day 1" 0.9 nm horizontal electron beam emittance and the projected 500 mA current was assumed at these calculations.

2.1.2 X-ray beam position monitor

Historically at NSLS-II, front-end XBPMs[32] have not been uniformly installed; however, there is a benefit to these devices: they can be easily integrated into a feedback loop on the trajectory of the electron beam. This has been done at the Hard X-ray Nanoprobe to good result and we will require similar beam stability for CDI, so we **propose to install front-end XBPMs**.

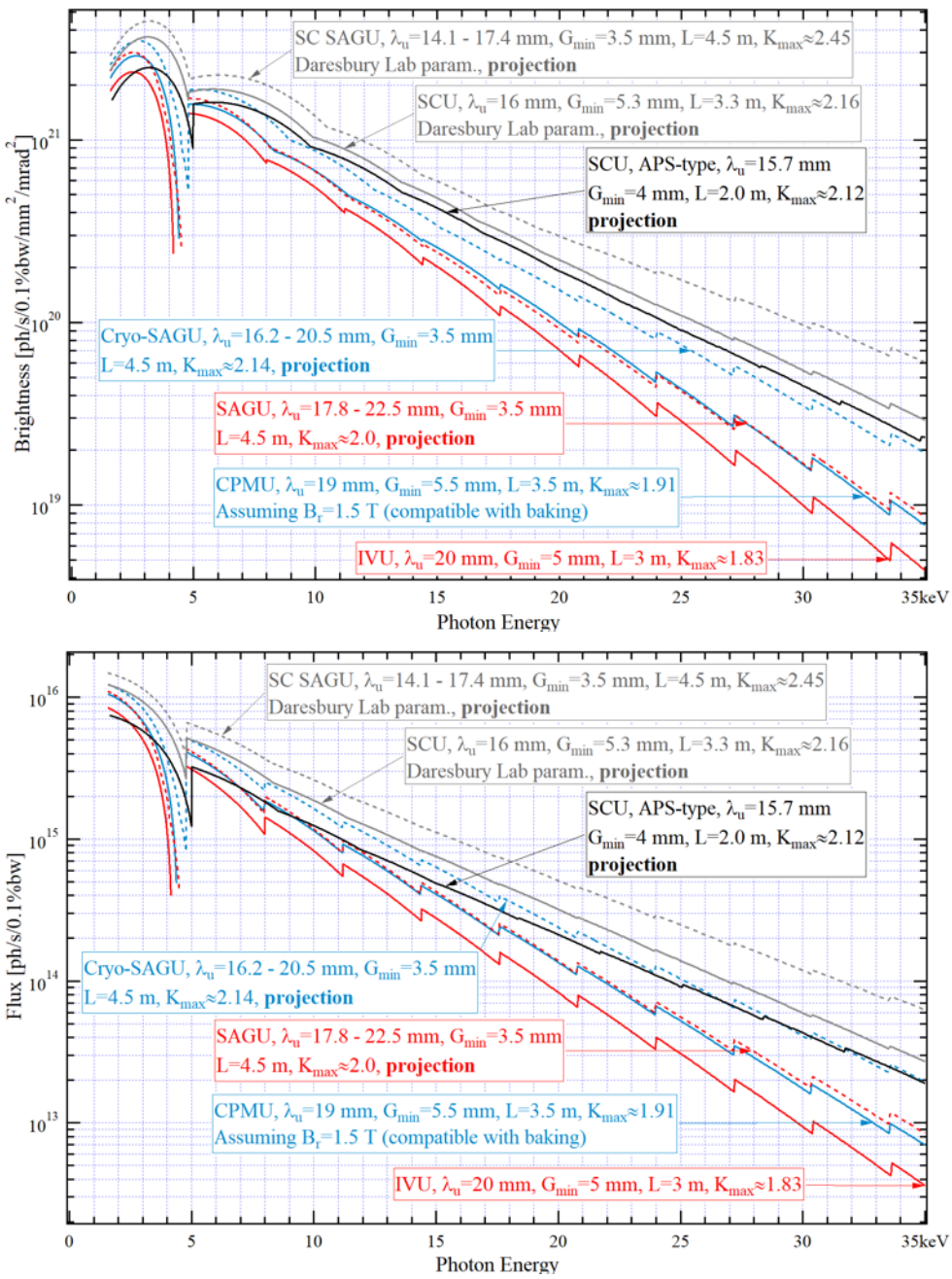

Figure 7: Approximate spectral brightness and flux curves of possible undulator options assuming different magnet technologies (IVU, CPMU, SCU), all satisfying spectral requirements of the Bragg CDI beamline. In addition to conventional undulator brightness and flux curves (solid lines), curves for eventual segmented adaptive-gap undulators (SAGU) for the corresponding magnet technologies are also shown (dashed lines). "Long-term goal" NSLS-II 0.55 nm horizontal electron beam emittance and 500 mA current was assumed.

2.2 Optical Simulations

The SR calculation method implemented in the SRW code is based on the retarded potentials technique and allows for high-accuracy CPU-efficient computation of the horizontal and vertical components of the frequency-domain electric field generated by a relativistic electron in a magnetic field of arbitrary configu-

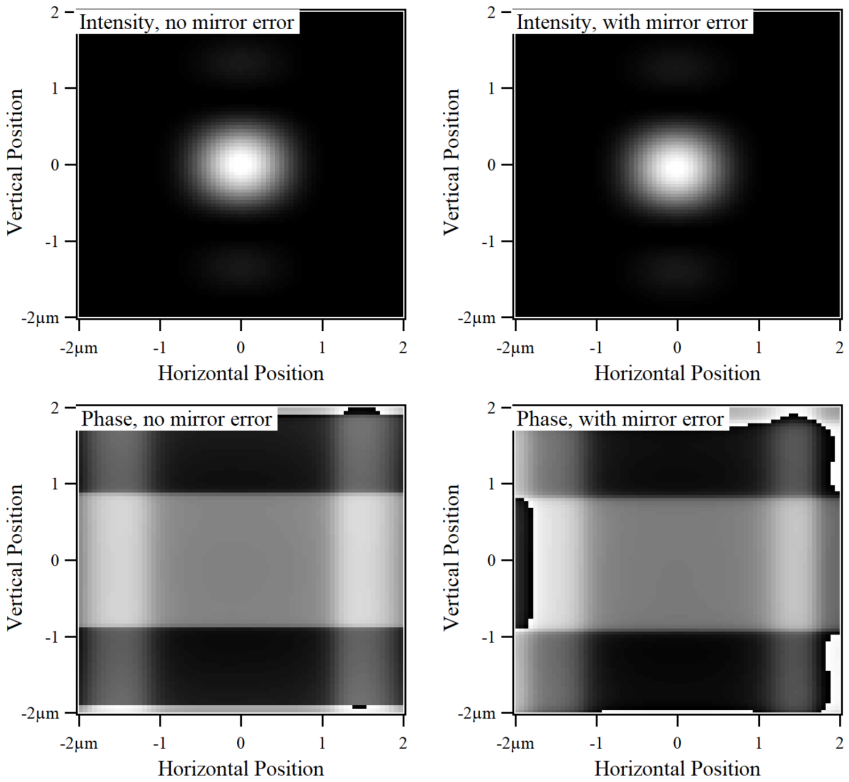

Figure 8: Intensity distributions (upper image plots) and principal value of the phase (lower image plots) of undulator radiation electric field from single electron propagated to sample position, without (on the left) and with (on the right) possible mirror errors, for the 100 m beamline option, 1 um spot size case, see Fig. 12

ration as observed in the near-field region [27]. The simulation of propagation of a fully-coherent radiation beam is implemented using a combination of the CPU-efficient Fourier optics, the stationary phase, and the X-ray dynamical diffraction based methods. For each optical element and drift space, the propagation of two transverse components of the frequency-domain electric field is simulated locally, from a plane perpendicular to the optical axis before the element, to a plane perpendicular to the optical axis after it. The intensity, as well as the mutual intensity or cross-spectral density, of the partially-coherent radiation from the entire electron beam is calculated by summing up intensities derived from electric fields emitted by different "macro-electrons" distributed over the phase space of the electron beam and propagated through an optical system to a required observation plane[33]. This calculation method was successfully used for estimating performances of early coherence-exploiting beamlines at NSLS-II[34] and for preliminary simulations for the Bragg CDI beamline[35].

2.3 60-m optical scheme

A "short" version of our four-mirror zoom concept is illustrated in Fig. 10, where the top panel displays the optical components and their locations to produce a 1-micron focal spot with a coherence length roughly equal to the beam size. The monochromator, not shown, would be located upstream of the slit labeled 'S0.' For each of the two schemes, the radius of curvature of the first two mirrors change as the focal spot size is changed. These mirrors produce a secondary source, where the horizontal and vertical sources are not coplanar. That source is reimaged by the final, fixed figure mirror optics onto the sample, located 60 m from the source. Note that the final horizontal and vertical mirrors must be moved to keep the "zoomable" focus at the waist of the x-ray beam. The parameters for these configurations are shown in Fig. 14. The transverse

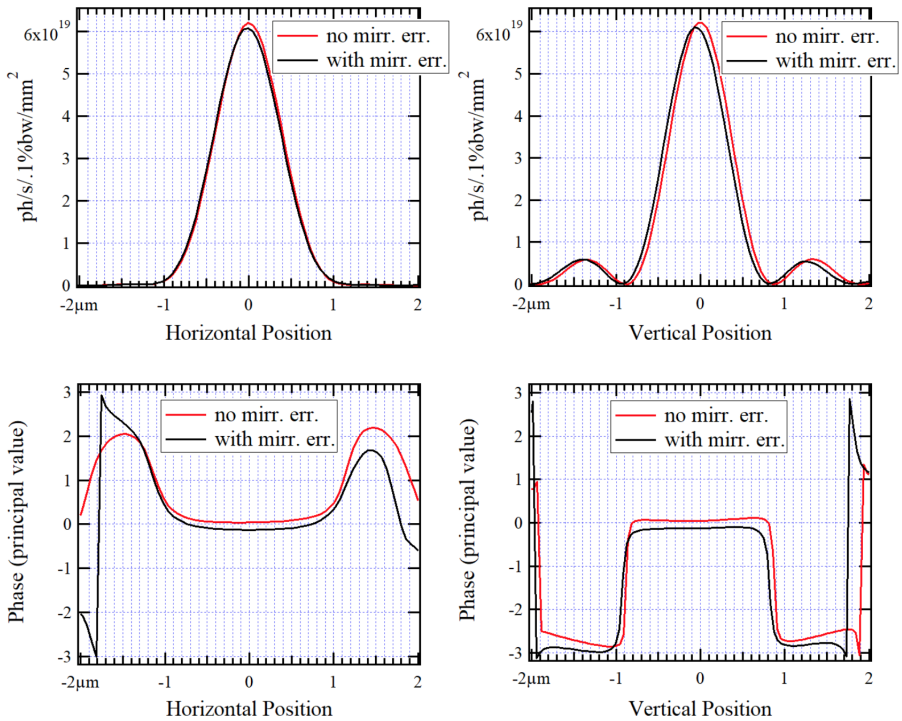

Figure 9: Central cuts of intensity distributions vs horizontal (left) and vertical (right) position (upper plots) and the corresponding principal value of the phase (lower plots) of undulator radiation electric field from single electron propagated to sample position, without and with possible mirror errors, for the 100 m beamline option, 1 um spot size case, see Fig. 12

coherence properties of the x-ray beam can also be altered by closing apertures along the beam path. As the x-ray field becomes increasingly coherent, the divergence added by small apertures can be counteracted by changing the curvature of the first two mirrors. As discussed below, *this option is possible only at Sector 29-ID.*

Fig. 12 summarizes our simulation for the 60-m concept providing a 1 micron focus with coherence length matched to the beam size, while Fig. 13 demonstrates the ability to provide a 10 micron spot with little change in the total number of photons in the focus. At the top of each figure is a a schematic optical design, neglecting the monochromator, followed by the partially coherent horizontal and vertical beam profiles, the simulation of the coherence function in each direction, and the location of the beam waist with respect to the sample position, denoted 0 m on this plot. *To bring the sample to the waist of the x-ray beam in any of these simulations, it is necessary to move the final focusing mirrors.*

2.4 100-m optical scheme

The 100-m long conceptual design is very similar to the shorter version discussed above. This design requires that the endstation be placed in a satellite building to the facility. Additional information concerning this building is discussed in Section 5. Figs. 12 and 13 demonstrate the layout and present the simulations that assure that the optical scheme works as expected.

2.5 Comparison of optical designs

Fig. 14 provides the detailed parameters for the optical simulation. We note that the required bending radius of either of the two mirrors is rather modest. In both designs, the final slits must be rather narrow,

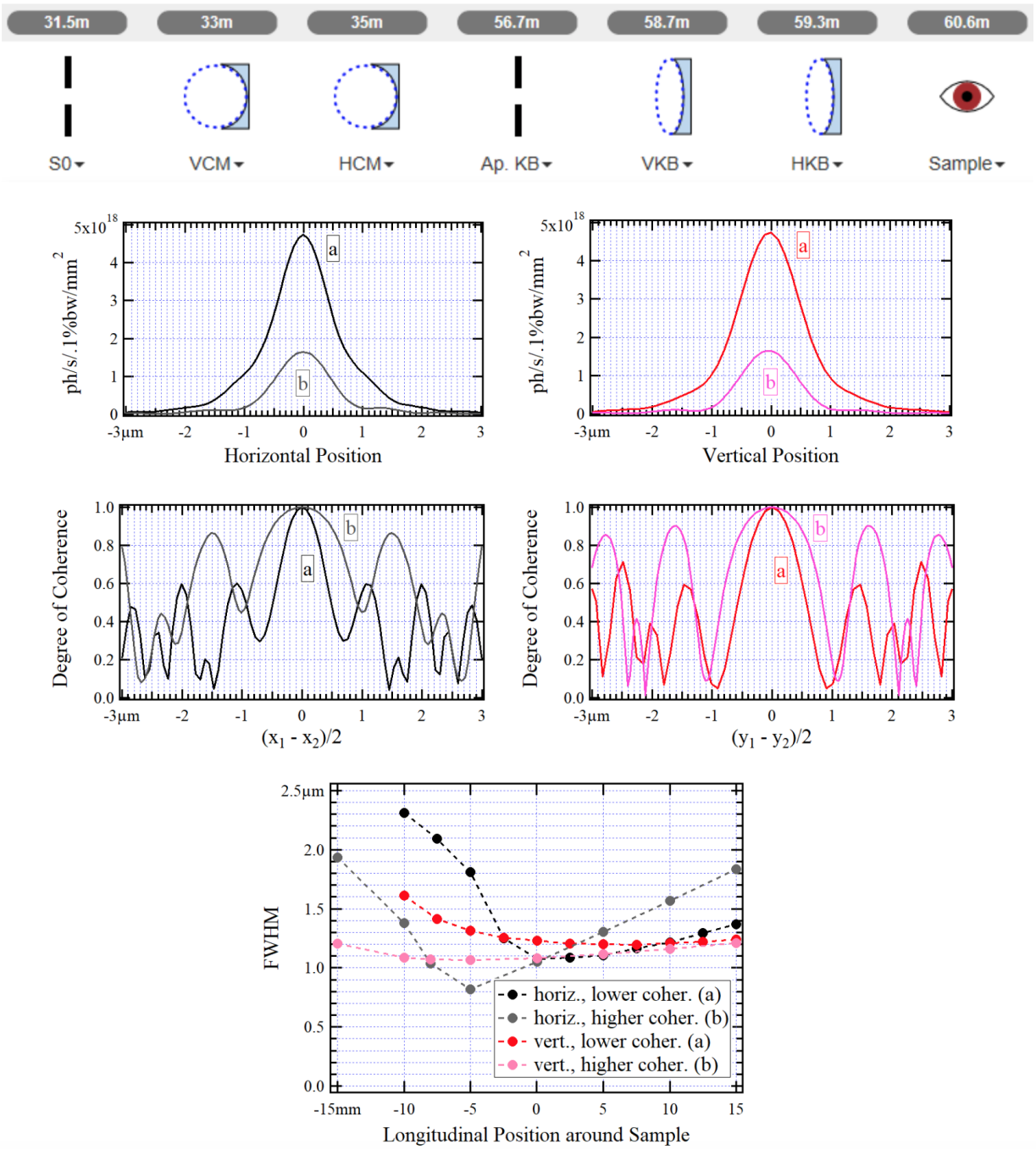

Figure 10: Results of partially-coherent 8 keV undulator radiation propagation calculations for the 60 m beamline layout optimized for 1 um spot size at sample (scheme at the top): horizontal and vertical central cuts of intensity distributions (upper plots), degree of coherence in the horizontal and vertical directions (middle plots) at the sample position, and the horizontal and vertical FWHM spot sizes as functions of the longitudinal offset from the sample position (lower plot). The calculations were done for a "lower" (a) and "higher" (b) coherence cases, when the transverse coherence lengths at the sample are 1 um and 2 um respectively.

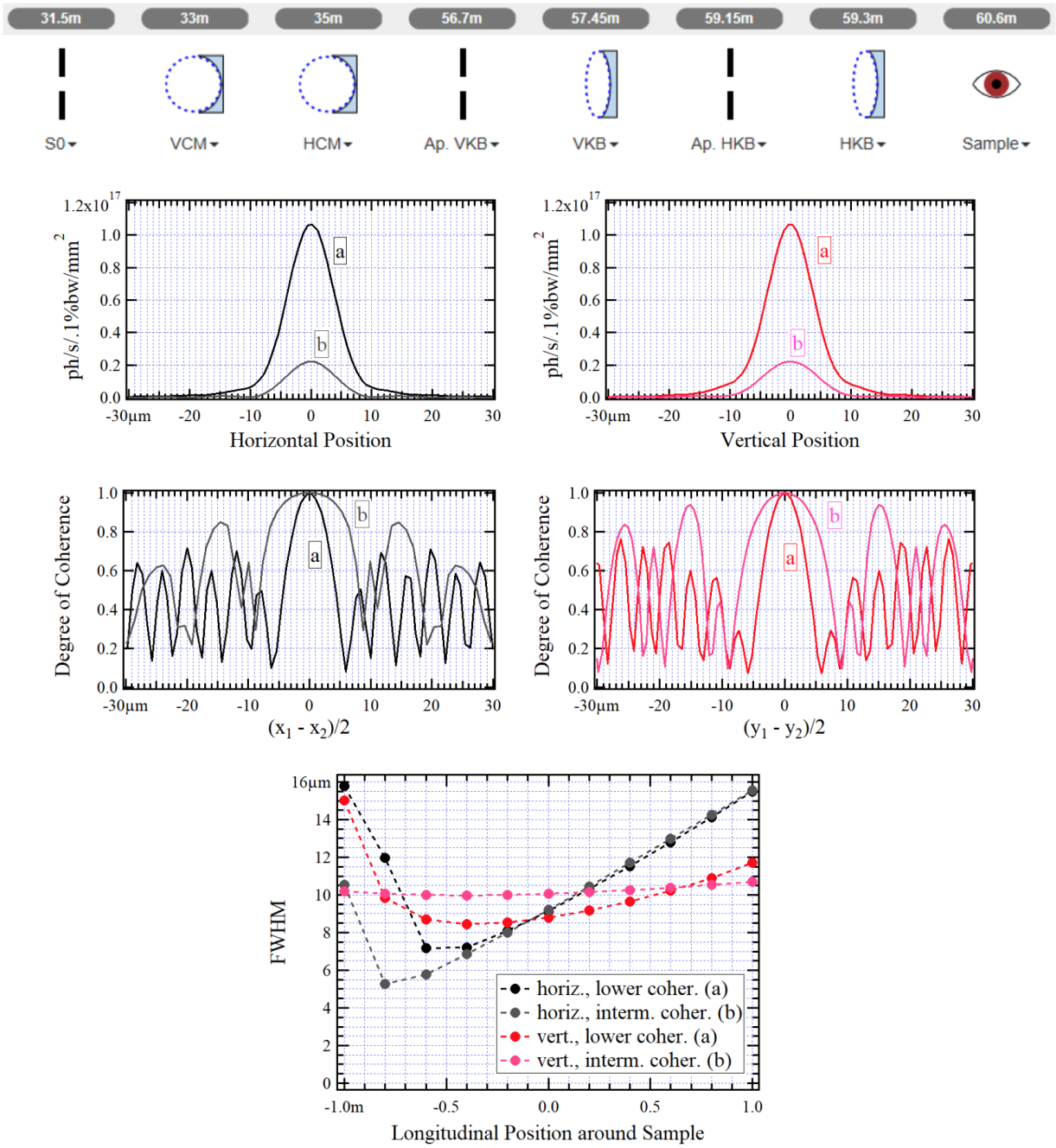

Figure 11: Results of partially-coherent 8 keV undulator radiation propagation calculations for the 60 m beamline layout optimized for 10 um spot size at sample (scheme at the top): horizontal and vertical central cuts of intensity distributions (upper plots), degree of coherence in the horizontal and vertical directions (middle plots) at the sample position, and the horizontal and vertical FWHM spot sizes as functions of the longitudinal offset from the sample position (lower plot). The calculations were done for a "lower" (a) and "higher" (b) coherence cases, when the transverse coherence lengths at the sample are ∼10 um and >15 um respectively.

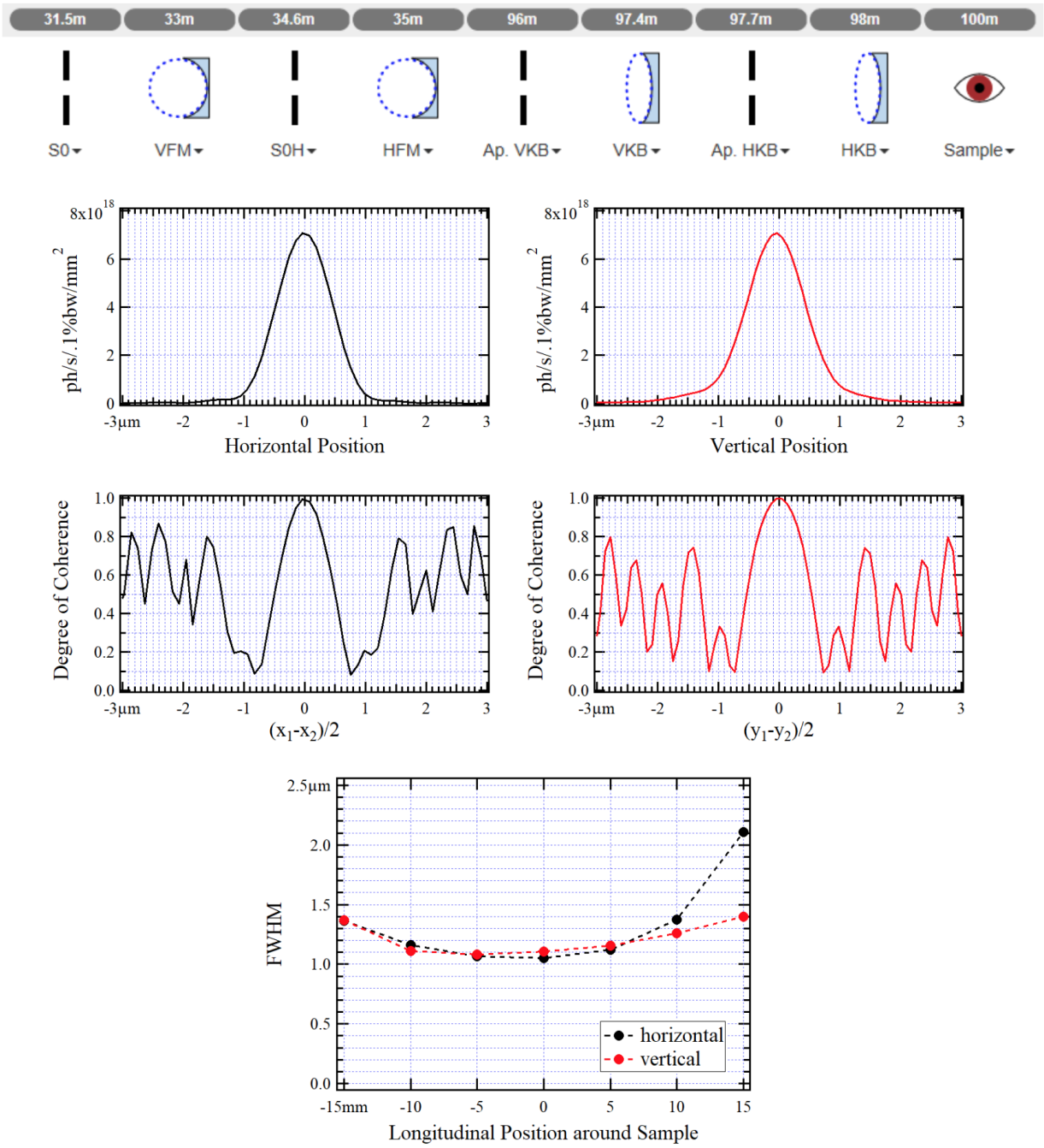

Figure 12: Results of partially-coherent 8 keV undulator radiation propagation calculations for the 100 m beamline layout optimized for 1 um spot size at sample (scheme at the top): horizontal and vertical central cuts of intensity distributions (upper plots), degree of coherence in the horizontal and vertical directions (middle plots) at the sample position, and the horizontal and vertical FWHM spot sizes as functions of the longitudinal offset from the sample position (lower plot). Mirror surface height error was derived from the optical metrology data on actual mirrors installed at LCLS.

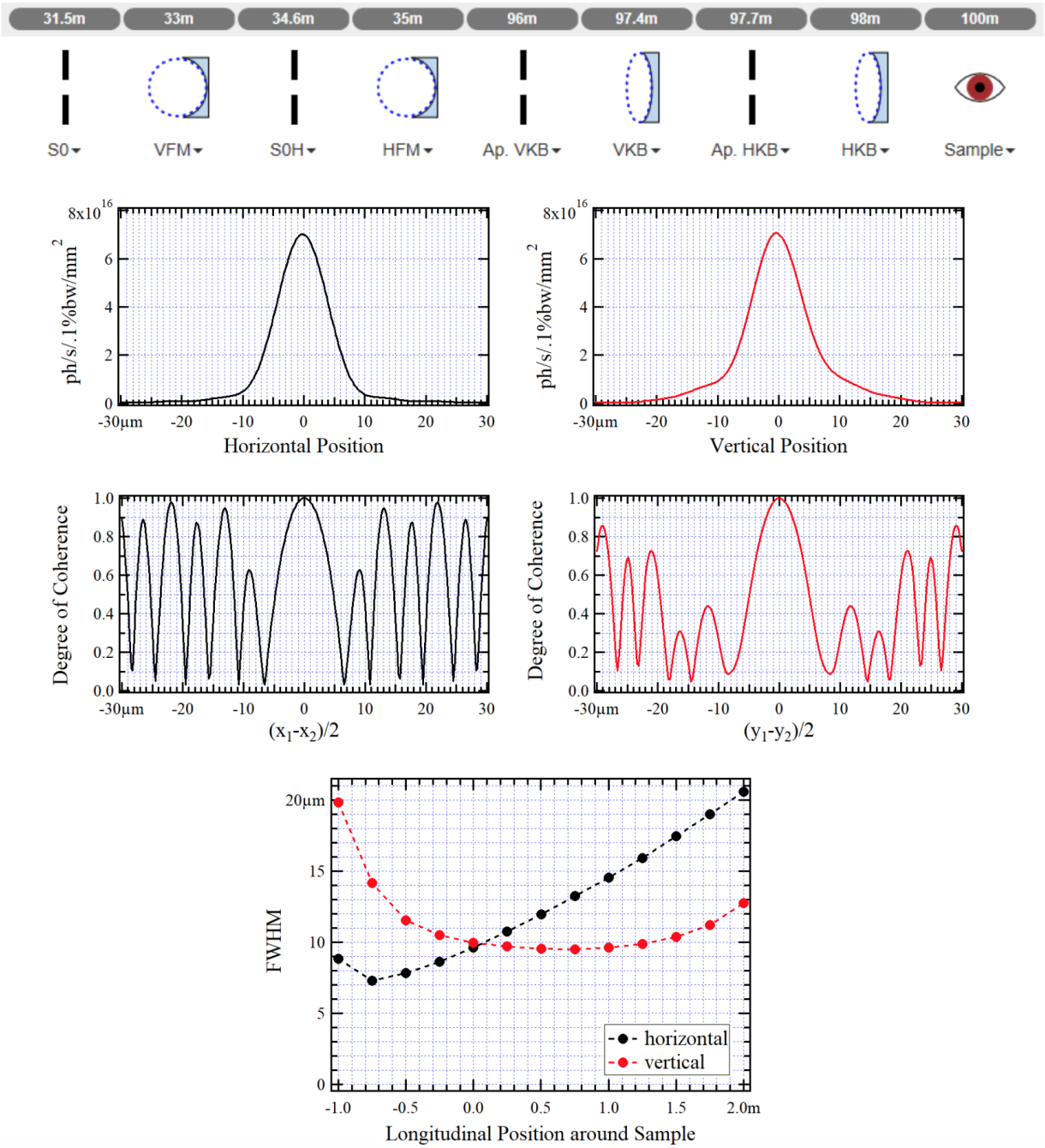

Figure 13: Results of partially-coherent 8 keV undulator radiation propagation calculations for the 100 m beamline layout optimized for 10 um spot size at sample (scheme at the top): horizontal and vertical central cuts of intensity distributions (upper plots), degree of coherence in the horizontal and vertical directions (middle plots) at the sample position, and the horizontal and vertical FWHM spot sizes as functions of the longitudinal offset from the sample position (lower plot).

Layout Option	Δy_{S0} [μm]	$\Delta x_{S0(H)}$ [μm]	$r_{y\ VFM}$ [km]	$r_{x\ HFM}$ [km]	Δy_{AKB} [μm]	Δx_{AKB} [μm]	z_{VKB} [m]	z_{HKB} [m]	$p_{y\ VKB}$ [m]	$q_{y\ VKB}$ [m]	$p_{x\ HKB}$ [m]	$q_{y\ HKB}$ [m]	F ph/s/ .1%bw
60.6 m BL length ~1 μm spot ~1 μm coh. len.	420	35	12.20	5.00	1000	1000	58.70	59.30	10.25	1.90	21.767	1.308	1.0e13
60.6 m BL length ~1 μm spot ~2 μm coh. len.	210	17.5	10.40	5.00	1000	1000	58.785	59.31	10.25	1.90	21.767	1.308	2.7e12
60.6 m BL length ~10 μm spot ~10 μm coh. len.	800	400	14.80	12.00	50 @56.7m	25 @59.2m	57.45	59.30	10.25	1.90	21.767	1.308	1.0e13
60.6 m BL length ~10 μm spot ~15 μm coh. len.	800	70	14.80	12.00	25 @56.7m	20 @59.2m	58.15	59.30	10.25	1.90	21.767	1.308	2.6e12
100 m BL length ~1 μm spot ~1 μm coh. len.	400	46	18.7	9.58	1000	400 @97.7m	97.40	98.00	32.0	2.60	58.00	2.00	1.0e13
100 m BL length ~10 μm spot ~10 μm coh. len.	800	400	23.6	37.0	45 @96.0m	35 @97.7m	97.40	98.00	32.0	2.60	58.00	2.00	1.0e13

Figure 14: Main parameters of optical elements for which the calculations illustrated in Figs. 10-13 were performed. Details on the mirror geometry can be found in Section 2.10.

reinforcing the need for positional stability of the components with respect to one another and the sample. Examining Figs. 10 to 13, we see that in order to remain in the waist of the x-ray beam, it is necessary to move the mirrors. The minimization and impact of this movement is the subject of on-going simulations. The total range of the required motion is on the order of 500 mm.

2.6 Comparison of floor plans

During the course of the beamline development project, we have considered multiple sites at NSLS-II at which this beamline could be located. Fig. 15 shows a concept of the beamline positioned at 29-ID on the experimental floor. The hutch occupies the 29-ID, 30-BM, and roughly half of the 30-ID slots on the floor. Sector 30 is the injection point for the storage ring, so development of independent beamlines for these sectors is unlikely. The floor space at 30-ID is currently used for the Synchrotron Light Monitor diagnostic used by the accelerator staff to insure ring stability. Placing the hutch at this location would trigger a redesign effort to relocate the diagnostic.

The proposed experimental hutch is much larger than any other built on the experimental floor. An engineering concept for a hutch roof with this large unsupported span has not been undertaken. The hutch footprint as drawn is not feasible, given the proximity of the detector support to the by-pass corridor and the load-limit on the fringes of the experimental floor. A further design effort would be required. This is likely to result in either a reduction in the sample-to-detector distance or a redesign of of the optical system and a reduction of the angular coverage of the detector motion system. It is unclear how vibrational stability would be ensured in this design. Environmental issues are addressed in more below, but vibrational noise is a significant concern on the experimental floor.

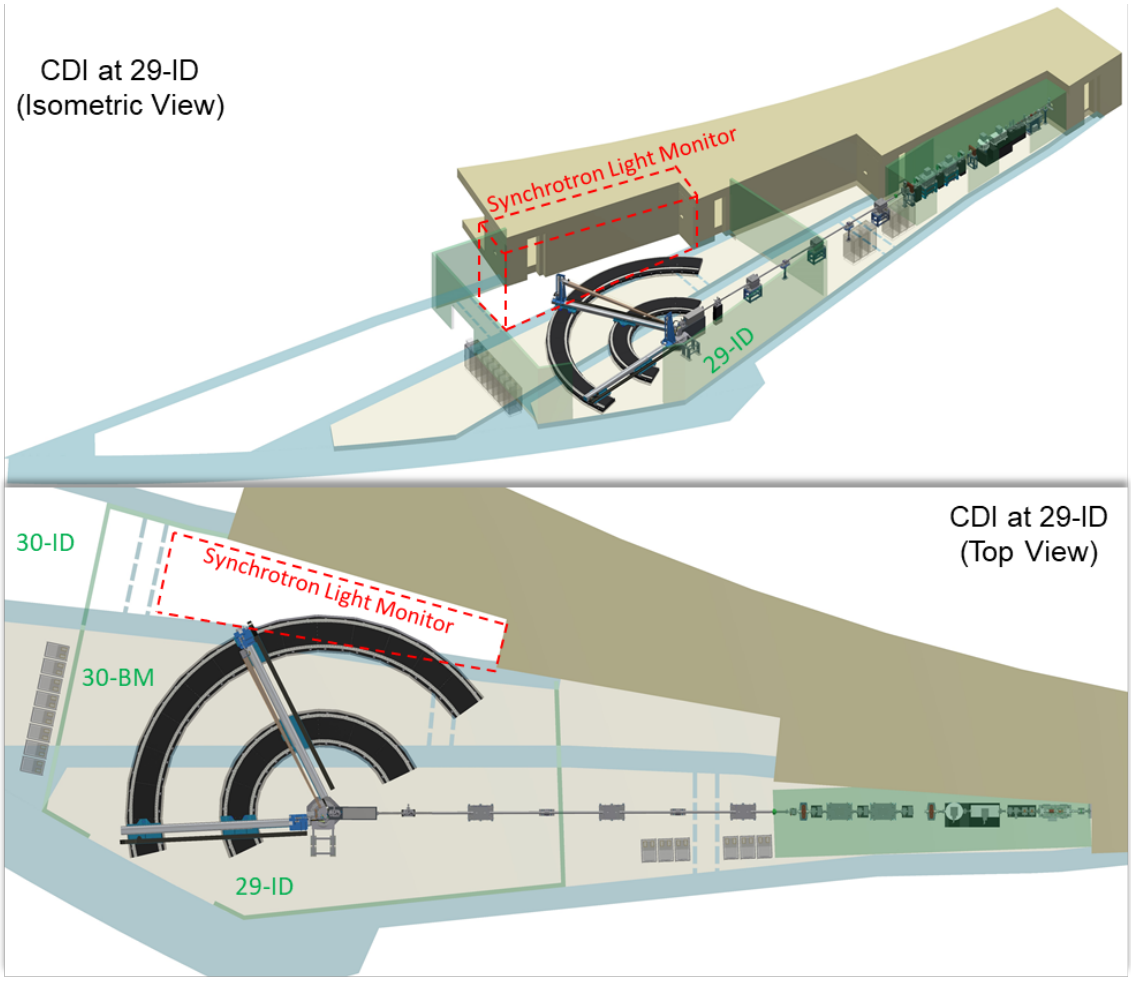

Figure 15: A schematic floor layout that represents a best fit between our 60-m optical design and the available space on the NSLS-II experimental floor. Note that since the original drafting of this concpet, it has become clear that the detector support cannot be this near to the access corridor surrounding the experimental floor.

These considerations, and the environmental concerns discussed in discussed in Section 3.3, lead us to advocate for a 100-m-long concept. Here, the endstation is located in a dedicated satellite building at 9-ID (Additional information is provided in Section 5.) and is connected to LOB 4, much as HXN is connected to LOB 3. In this design–see Fig. 16–there is ample clearance for the arc of the detector motion system. Disruption to current and future activities on the experimental floor is minimized and the environmental factors affecting stability, both thermal and vibrational, can be assumed to be similar to those at HXN, the NSLS-II beamline that has the most in common with the proposed project. In this preferred concept, the monochromators, the first mirror pair, and related diagnostics will be located in hutch adjacent to the NSLS-II shield wall. A small diagnostic enclosure, housing a "pop-in" destructive beam visualization screen and a transmissive beam position monitor, would be located near the edge of the experimental floor. The final focusing optics would be housed in a satellite building with the sample and detector positioning systems.

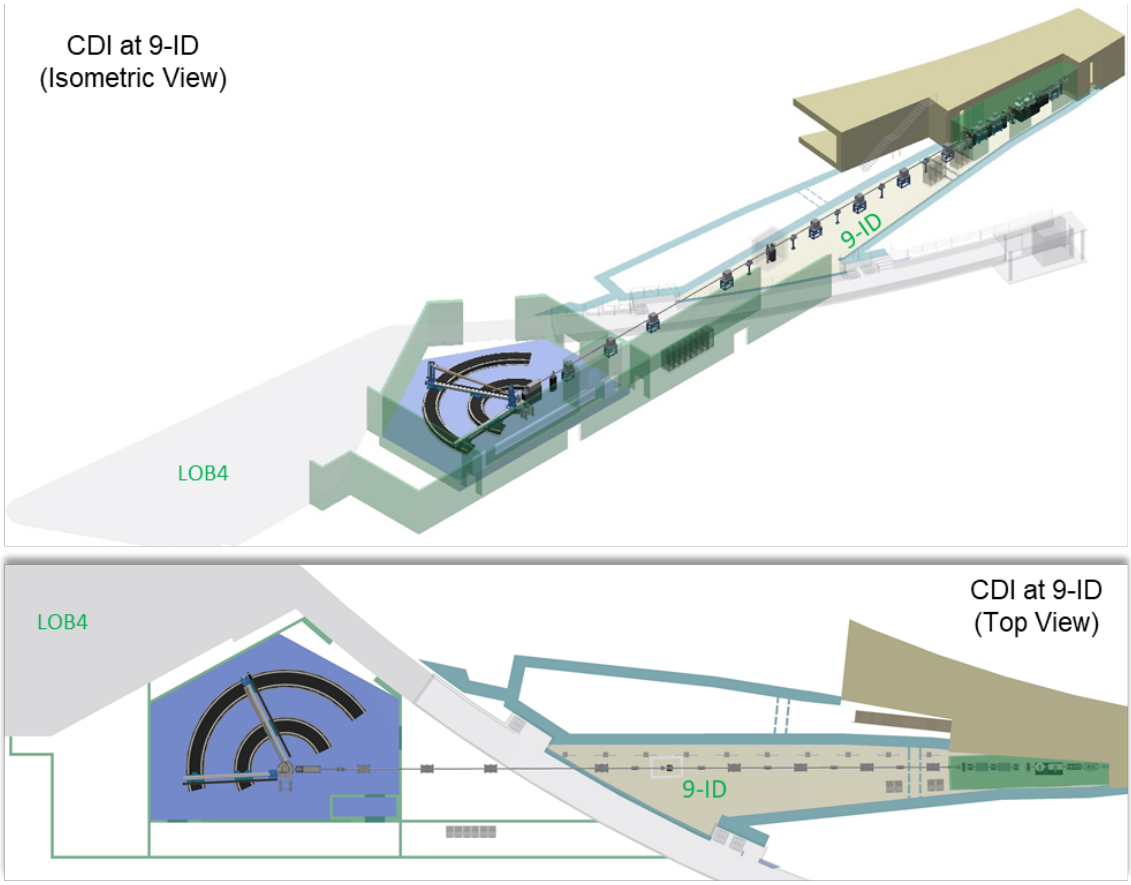

Figure 16: A floor layout that represents a best fit between our 100-m optical design with the experimental station housed in a satellite building.

2.7 Fundamental harmonic filter

NSLS-II is a 3-GeV storage ring and, as such, an undulator's fundamental harmonic energy is typically below below our lowest design energy of 5 keV. Given the requirements on the optical design, namely, to avoid unnecessary phase structure in the x-ray field, we propose to reduce the thermal load on our optical components by introducing a filter to preferentially absorb the low energy undulator emission. A diamond filter made through chemical vapor deposition would transmit about 88% of 5 keV radiation and less than 10% of that at 2 keV or below. Fig. 17 demonstrates this. The finite element analyses in the following sections reference performance with this filter in place.

	100-m concept impact	60-m concept impact
Endstation location	In a satellite building adjacent to the main building.	On the experimental floor at Sector 29-ID.
Optical design considerations		
Beam pointing stability	Stability requirement demands feedback system.	Stability requirement demands feedback system.
Mech. design considerations		
Space requirements	Ample space to design an unconstrained geometry to meet the science needs.	Constraints exist on the experimental floor: 8-m detector arm may not be feasible, accelerator device must be redesigned and relocated.
Vibrational stability	Due to its location in a satellite building, there is a high likelihood that requirements could be met on week days with controlled access to the hutch. Can expect very good correlation in floor motion over relevant length scales.	On the experimental floor, there is a high likelihood that requirements could be met at night and on Sundays and holidays.
Temperature stability	Stability of $\pm 0.1\,^{\circ}\mathrm{C}$ in the similarly-designed HXN hutch.	Typical hutch performance is $\pm 0.5\,^{\circ}\mathrm{C}$.
Logistics	1. Hutch construction procedure is well-understood.	1. Hutch is large and the detector system is heavy. May require additional study. 2. Synchrotron Light Monitor needs to be redesigned.

Table 1: A comparison of logistical considerations for the 60- and 100-meter designs

2.8 Slits

In the above optical design, the control of the final x-ray spot size and the spatial coherence properties of the field are varied by coordinated changes in optics and aperture sizes. Only one pair of slits will see the white beam in our optical scheme and this aperture will be relatively large. We will base the design on facility experience, for example, the NSLS-II design for the HXN white beam slits, whose performance has been adequate.

The slits in the monochromatic beam will all be of high quality to minimize the impact of any unintended diffraction from imperfections. Fortunately, the quality of slit blades for x-ray apertures has increased dramatically during the last two decades, most recently driven by the demands of high-brightness sources, and both highly polished and single crystal blades are commercially available from multiple vendors.

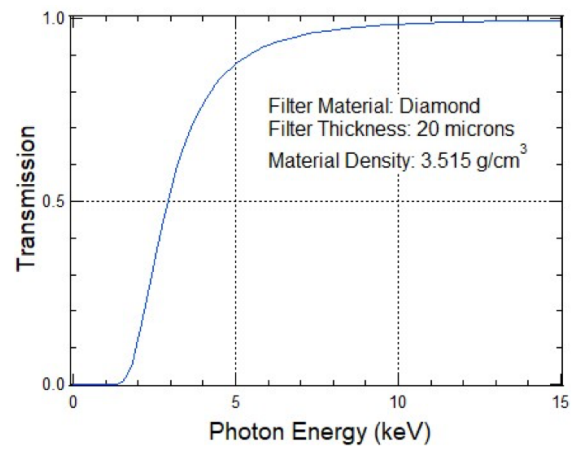

Figure 17: The transmission of x-rays through a diamond filter of thickness 20 microns. This device will reduce heat-load on the optics at the cost of a small reduction in x-ray flux.

2.9 Monochromators

The monochromator will determine the temporal, or longitudinal, coherence length over an energy range of 5-15 keV. To a first approximation, in CDI we require that the path length difference of the rays passing through the extrema of a sample and interfering at the detector be shorter than[36]: $l_c^{long} > d\tan(\theta)$, where d is the size of the crystal and θ is the largest scattering angle measured(We define the coherence length following Mandel and Wolf, Sec 4.2[37].). For example, to measure a (111) reflection from a gold crystal of 1 micron diameter with 8 keV incident photon energy, we require $l_c^{long} > 0.35$ microns.

To reduce the heat load on the bendable mirror pair in our optical scheme, we place the monochromator in the white beam. The heat load will deform the crystal, but this load is expected to be relatively constant since we do not plan to change the photon energy by more than a few hundred eV during a CDI measurement.

The CDI monochromator, located approximately 30 meters from the center of the CDI insertion device straight section, consists of one Double Multilayer Monochromator (DMM) and one Double Crystal Monochromator (DCM) mounted on a common granite base. The 30 meter dimension is from the source point to the center of the first multilayer in the DMM. The DCM will provide two pairs of silicon crystals, Si(111) and Si(311), to cover the 5-15 keV photon energy range. The incoming white beam is horizontally diffracted, with a 20 mm fixed offset, by either one pair of multilayer mirrors or one pair of silicon crystals, see Fig. 18. The DMM and DCM optics are mounted on platforms in their vacuum chambers. The platform rotation axes, in the y-direction, are located at the centers of the first optical elements surfaces and the lengths of the 2nd optical elements are set to accept the shifting beam footprint as the monochromator energy is changed over its full range.

In the DCM mode of operation shown in Fig. 19(right), the multilayer mirror pair is moved out of beam path by a horizontal translation perpendicular to the first multilayer mirror surface when the DMM Bragg angle is set to zero, defined as the alignment position. In the DMM mode of operation shown in Fig. 19(left), the vertical translation of the DCM crystal cages is set to a gap between the crystal pairs. This translation is used to select either the Si(111) or the Si(311) crystal pairs during DCM operation. In this way, the same region of a sample can be interchangeably measured with either the wide-bandpass DMM or the narrow-bandpass DCM, allowing for the best matching of source properties to the needs of the measurement.

2.9.1 Double crystal monochromator

We propose, as the primary monochromator, a fixed-offset double crystal monochromator equipped with two pairs of crystals: Si(111) and Si(311). The longitudinal coherence length of the radiation passing the

Bragg Angle Rotation Platform

DoF	Range	Repeatability	Resolution	Stability
Bragg Angle*,†	$-1°$ to $5°$	<1.0 µrad	<0.25 µrad	<0.2 µrad

*Rotation Center: center of the first multilayer surface along Z direction, around Y axis.
†Operating range is 1.1° - 3.6°.

The 1st multilayer orientation

DoF	Range	Repeatability	Resolution	Stability
Fine Pitch	±500 µrad (Rocking Curve Scanning)	<0.5 µrad	<0.1 µrad	<0.1 µrad
Fine Roll	±1°	<2.0 µrad	<0.5 µrad	<0.1 µrad
X Translation	−9 mm to 1 mm	1 µm	0.5 µm	-

The 2nd multilayer orientation

DoF	Range	Repeatability	Resolution	Stability
Coarse Yaw	±2° (with manual locker)	-	<2.0 µrad	-
Coarse Roll	±2° (with manual locker)	-	<2.0 µrad	-
X Translation, fine	±0.1 mm	<0.5 µm	<0.1 µm	<0.2 µm

Table 2: Specifications for DMM motions.

Bragg Angle Rotation Platform

DoF	Range	Repeatability	Resolution	Stability
Bragg Angle*,†	$-1°$ to $52°$	<2.0 µrad	<0.5 µrad	<0.2 µrad
Y Translation	±50 mm	<10 µm	<1 µm	<1 µm

*Rotation Center: center of the first crystal surface along Z direction, around Y axis.
†Operating range is 7° - 50°.

The 1st multilayer orientation

DoF	Range	Repeatability	Resolution	Stability
Fine Pitch	±200 µrad (Rocking Curve Scanning)	<1.0 µrad	<0.2 µrad	<0.1 µrad
Fine Roll	±1°	<2.0 µrad	<0.5 µrad	<0.1 µrad

The 2nd multilayer orientation

DoF	Range	Repeatability	Resolution	Stability
Coarse Yaw	±2° (with manual locker)	-	<2.0 µrad	-
Coarse Roll	±2° (with manual locker)	-	<2.0 µrad	-
X Translation, fine	−0.5 mm to 7 mm	<1.0 µm	<0.2 µm	<0.2 µm

Table 3: Specifications for DCM motions.

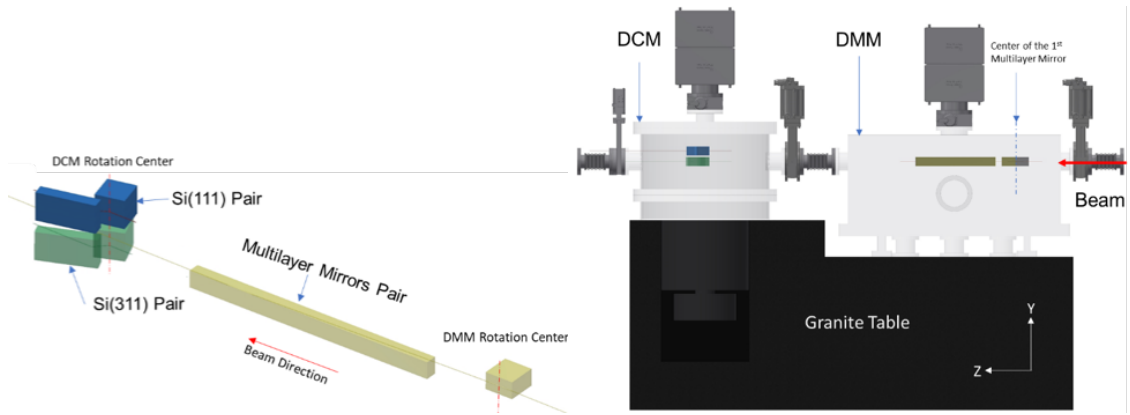

Figure 18: (left) CDI Monochromator Optics Scheme and (right) layout elevation view, viewed from the outboard side.

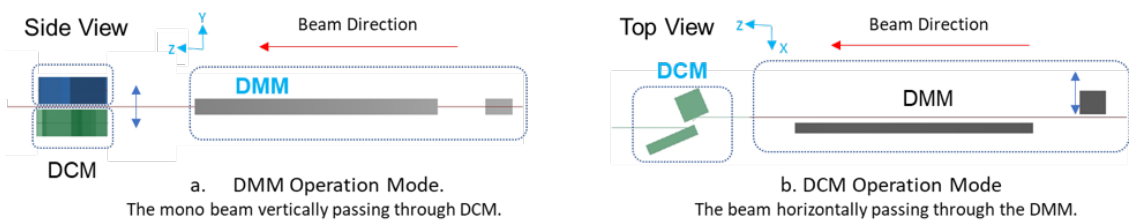

Figure 19: DCM and DMM Operation Modes

monochromator depends on the wavelength, λ, the Darwin width, ω_0, and the Bragg angle, θ_B, of the reflection[38]: $l_c = \lambda^2/\partial\lambda = \lambda \tan(\theta_B)/\omega_0$. For our chosen crystals, these values are: $l_c^{\mathrm{Si}(111)} = 1.2$ microns at 8 keV; and $l_c^{\mathrm{Si}(311)} = 5.6$ microns at 8 keV. We expect that the Si(111) crystals will be sufficient for routine operation and the Si(311) will permit the study of large crystals and high-order reflections.

2.9.2 Horizontal vs vertical deflection

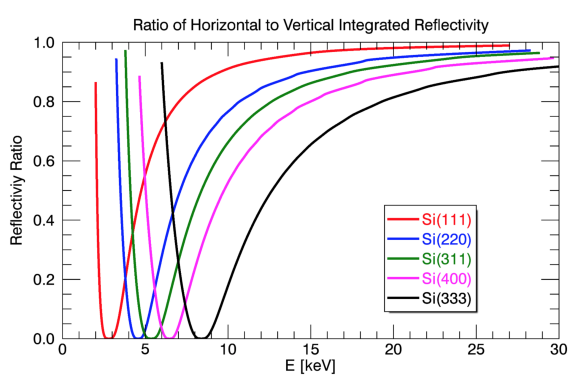

Figure 20: The reflectivity ratio of various Si reflections when horizontally polarized x-rays are incident upon a horizontally deflecting monochromator due to the narrowing of the energy band-pass.

We propose to use a conventional source, i.e., the radiation produced will be horizontally polarized. Additionally, we expect that the performance of this beamline will be sensitive to beam motion and we propose a cryogenically cooled crystal monochromator. Horizontally deflecting monochromators tend to provide higher beam stability, since the primary rotation is about the vertical axis. This feature, generally, allows for less excitation of the vibrational modes of the device by the vibrations of the ambient environment.

This geometry reduces the reflectivity of the device, due to the polarization dependence of the Darwin curve. These concerns have recently been addressed in a technical note prepared in conjunction with Advanced Photon Source upgrade project[39]. Fig. 20 shows the relative reflectivity of a horizontally deflecting monochromator with respect to a vertically deflecting one. For example, a Si(111) monochromator reflects approximately 50% as much light as a vertically deflecting one, with the ratio grow-

ing to 85% at 8 keV, and more than 90% above 10 keV. Si(311) crystals reflect less, reaching only 40% the performance of a vertically deflecting device at 8 keV. Since our general use-case for Si(311) is to support the measurement of large crystals, we expect that these samples will require the use of higher photon energies, to allow for absorption. While the above is certainly true, there is an additional consideration that is specific to CDI: because the reduction of the reflectivity is due to the narrowing of the Darwin width, the longitudinal coherence in these beams can become quite long, which is clearly beneficial for large samples. Our conceptual design proposes to **provide a double crystal monochromator with two pairs of silicon crystals, Si(111) and Si(311), in a horizontally deflecting geometry**.

2.9.3 Multilayers

A broader-bandwidth monochromatic beam ($\partial E/E \sim$1% or a bit less) is desired for locating and orienting grains within a polycrystalline sample, or for generally offering a more intense monochromatic beam for CDI measurements with adequate longitudinal coherence for the problem at hand. We plan to achieve this through use of a double multilayer monochromator that will be installed in the FOE adjacent to the double crystal monochromator, having the same offset as the latter and implemented in such a way such that one or the other monochromator is in use (with the one not in use being retracted from the beam path). A multilayer, or any Bragg diffractive optic, consisting of a stack of alternating heavy and light layers diffracts a bandwidth given by [40]: $B = Cd^2|F|/v$, where C is a proportionality constant, d is the d-spacing of the Bragg planes, F is the structure factor for the Bragg reflection, and v is the unit cell volume. The ratio of $|F|$ to v is simply an effective x-ray scattering density for the material and Bragg reflection at hand. Bandwidths diffracted by multilayers are larger than those diffracted by single crystals mainly by virtue of the larger d-spacings of multilayers, typically a factor of 10 bigger than for single crystals.

Large multilayer d-spacings imply shallower Bragg angles for multilayers compared with single crystals. Thus to preserve the same offset in a double multilayer monochromator as compared with a double crystal monochromator, the two multilayers must be spaced relatively far apart. For a desired offset of 20 mm, two multilayers having a 2 nm d-spacing must be spaced apart by 16 cm along the beam direction at 5 keV, by 32 cm at 10 keV, and by 48 cm at 15 keV. If the d-spacing is 2.5 nm, these separations increase to 20, 40, and 60 cm respectively. To achieve this inside a vacuum chamber, a mechanism which involves using a sine bar drive to change the angle of the multilayer pair is under consideration; the limited angle travel of a sine bar drive would be acceptable because the full energy range would be covered across less than 3°. We seek to employ water cooling of the first multilayer, that is struck by the white beam, to minimize vibrations. Finite element analysis (FEA) calculations indicate (See Table 4.) that acceptable thermal distortions of a multilayer are achievable for the incident white beam dimensions under consideration.

Metal-based multilayers consisting of metal or metal compound heavy layers, e.g., W, Ru, Mo, Pd, etc., and carbon/carbide or silicon/silicide light layers are commercially available and can be grown on smooth flat substrates such as silicon to dimensions exceeding tens of cm laterally. Hundreds of bilayers are typically deposited and the d-spacing of the bilayer can be anywhere from typically 2 nm to 5 nm or higher, with the thickness of the heavy layer typically being about one-fifth to one-half of the d-spacing. Interdiffusion between the light and heavy layers of the bilayers tends to limit the practical smallest d-spacing to be 2 nm, although d-spacings as small as 1.5 nm or less have been reported (See A. Rack et al.[41] for a review of multilayers used as monochromators in hard x-ray imaging applications.). An alternate route toward achieving narrower diffracted bandwidths for multilayers, typically 0.1%, involving minimal electron density contrast between the heavy and light layers of the bilayers has been explored, involving use of light metal oxides such as aluminum oxide as the heavy layer[42].

Calculations of the energy resolution and longitudinal coherence length using 2.5 nm d-spacing Mo-Si multilayers, with the thickness ratio of Mo:Si being 0.4:0.6, have been carried out. At 5 keV, the energy resolution would be 68 eV and the derived longitudinal coherence length would be 18.2 nm. These would be 136 eV and 9.0 nm respectively at 10 keV, and 205 eV and 6.0 nm respectively at 15 keV. For the case of 200 bilayers, the reflectivity of a single multilayer would exceed 60% at 5 keV, exceed 80% at 10 keV, and exceed 90% at 15 keV using the first order Bragg reflection; this assumes no interdiffusion between the layers. In the presence of interdiffusion between layers with a sigma thickness of 0.5 nm, the reflectivity would be reduced to around 30% at 5 keV, 60% at 10 keV, and 75% at 15 keV, while the diffracted bandwidths would narrow somewhat, thereby increasing the longitudinal coherence length.

Energy	Sagittal Slope Error		Longitudinal Slope Error	
	Peak-peak	RMS	peak-peak	RMS
5 keV	118.4 µrad	38.2 µrad	0.10 µrad	0.025 µrad
10 keV	36.10 µrad	11.7 µrad	0.12 µrad	0.029 µrad
10 keV	20.50 µrad	6.30 µrad	0.49 µrad	0.103 µrad

Table 4: The 1st multilayer mirror surface slope errors.

2.9.4 Monochromator offset

The DCM and DMM will provide the same offset of 20 mm of the monochromatic beam with respect to the incoming white beam. The offset will remain constant when changing x-ray energy. This offset is sufficient to ensure that white beam stops can be placed upstream of the mirror systems.

2.9.5 Finite element analysis of filter, DCM, and DMM

Upstream of the CDI monochromator, a 20 micron-thick diamond filter is inserted in the beam to filter out low energy photons. The maximum power transmitted by this filter is $\sim$ 185 W when the front end slits are set to 3 mm(Horizontal) $\times$ 1mm(Vertical) opening values. Fig. 21 shows the total power absorbed by the CDI monochromator at different energies and at different front end slit openings.

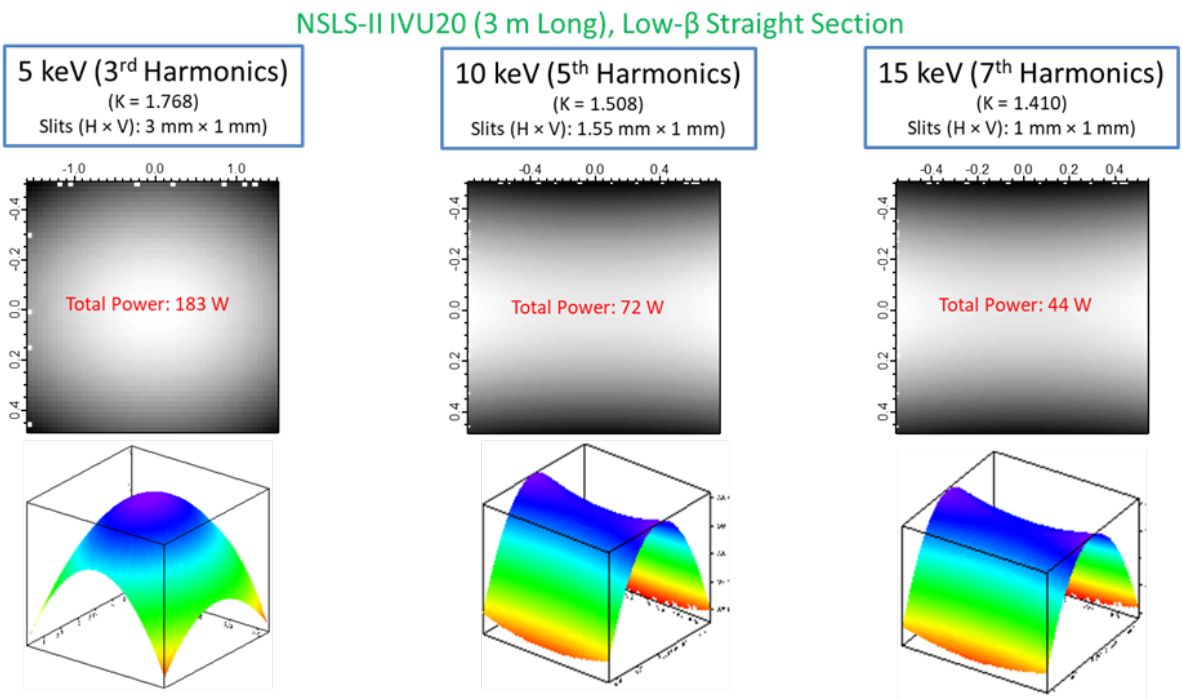

Figure 21: The Power Density Distribution after the CDI Filter

A new top-side water cooling scheme[43] is applied to the first multilayer mirror. The optics are fully illuminated by the beam in the longitudinal direction, which means that the size of the beam footprint in this direction is a constant 50 mm over the full energy range. Grooves cut into the multilayer mirror substrate just below the cooling channels are successfully able to isolate most of the mirror volume from the thermal distortion of the surface. The optimized substrate geometry with its cooling blocks is shown in Fig. 22.

Fig. 23 shows the CDI DMM 1st multilayer mirror temperature, displacement in X direction, and mechanical stress distributions for 5 keV, 10 keV, and 15 keV photon energies.

The optics surface profile of the 1st multilayer mirror is summarized in Fig. 24 and Table 4. Over the

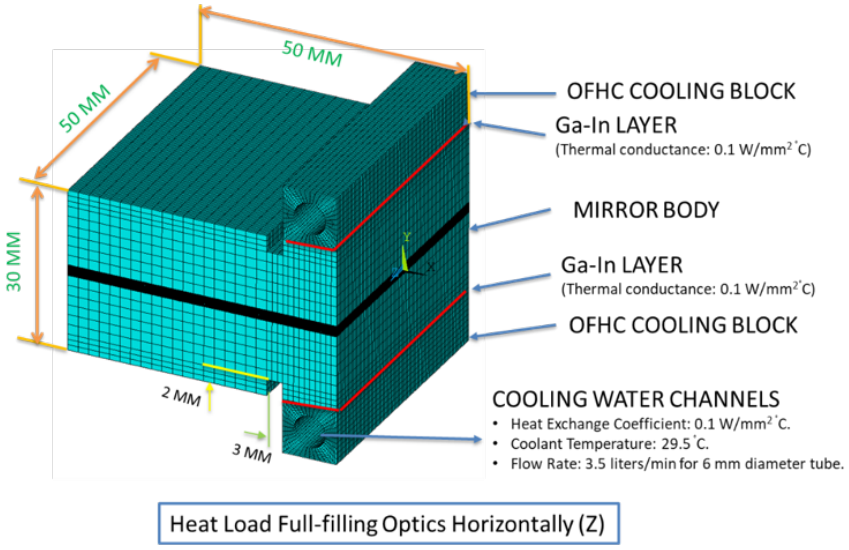

Figure 22: DMM 1st Multilayer Mirror Cooling Scheme

full photon energy range, the RMS longitudinal slope errors of the DMM multilayers are less than 0.11 µrad, and the worst-case RMS equivalent slope errors (taking Bragg angle value into account) are less than 2.4 µrad.

The classical indirect LN_2 cooling scheme is applied to the CDI DCM. To efficiently resolve heat load, the front end slit opening is set to 0.6 mm horizontal X 1mm vertical in order to limit the maximum absorbed power to less than 42 W at 5 keV photon energy. Fig. 25 shows preliminary FEA surface profile results for the 1st crystals of the CDI DCM. In the worst cases (largest Bragg angle, 5 keV), the surface slope errors are less than 1.7 µrad and 2.85 µrad for Si (111) and Si (311) respectively.

2.10 Mirrors

We have chosen to design our optical system around reflective optics, i.e., mirrors, to assure the achromaticity of the system. This is an important consideration due to the desire to exploit resonant contrast in complex samples and the need to acquire 3D Bragg CDI data by scanning the photon energy, which, in turn, is needed when the sample cannot be easily "rocked" to measure a full Bragg reflection, e.g., due to a large or complex environmental cell.

2.10.1 Pre-focusing optics

The first mirror pair in our optical scheme will provide relatively gentle focusing of the beam. As such the the requirements on the range over which the mirror radii change is roughly 5 to 40 km. We believe that this can be accomplished relatively easily with a standard bendable x-ray mirror. Our simulations were conducted with a figure error and height roughness that represents the best routinely achievable performance of commercial vendors.

2.10.2 Final focusing optics

This figures on this pair of mirrors will fixed. The performance of the beamline is most tightly specified by the performance of this mirror pair. We will pursue the best available mirrors for this system: < 0.15 nm mid-spatial frequency roughness and < 100 nrad slope error. As discussed below, these mirrors will have two stripes: one bare silicon and the other Cr.

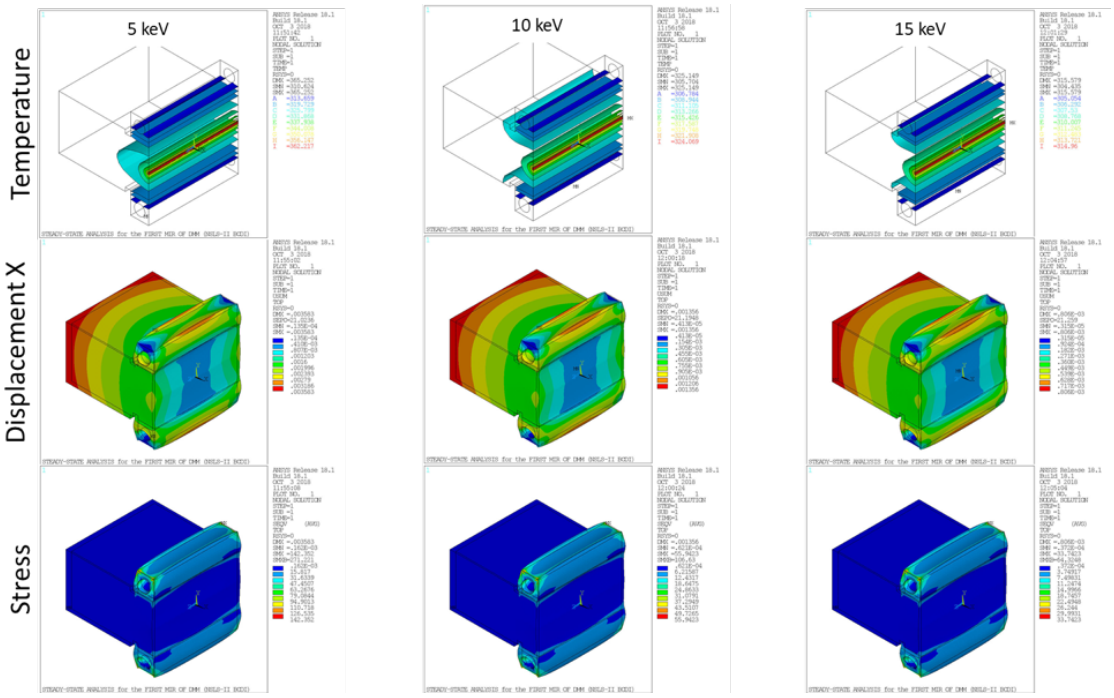

Figure 23: DMM 1st Multilayer Mirror temperature, Displacement and Stress Distributions

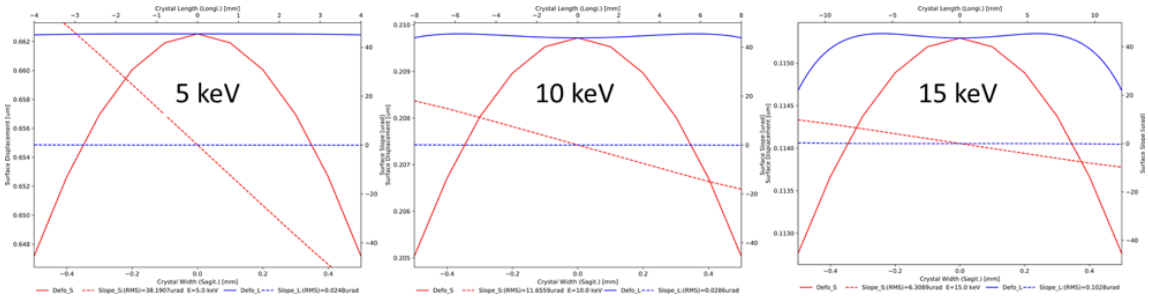

Figure 24: The 1st multilayer mirror surface profile thermal performance.

2.10.3 Incidence angles

In order to provide as much usable flux to the sample as possible, we propose a mirror system with relatively low angles of incidence. A plot is shown in Fig. 26, where the condensing mirrors make an angle of 1.75 mrad with respect to the beam emerging from the source and the final focusing optics 3 mrad with respect to their illuminating beam. Due to the low angle of the first mirror pair, these are proposed to be made from uncoated silicon. In the current design, our harmonic rejection is provided by the final focusing optics. While Rh is commonly chosen as a mirror coating, we propose to use Cr to provide additional harmonic rejection. **The final focusing mirrors are proposed to be silicon with a Cr stripe**. This system provides approximately 80% transmission over the beamline energy range, with nearly 85% transmission at 8 keV. Below 10 keV, Si would be the preferred mirror surface.

The harmonic energy rejection will be somewhat poor at the low energy end of the beamline's capability; however, harmonic contamination is rarely a significant problem in Bragg CDI data and most forward-scattering studies would be conducted at higher energies, where the transmission through the sample is higher.

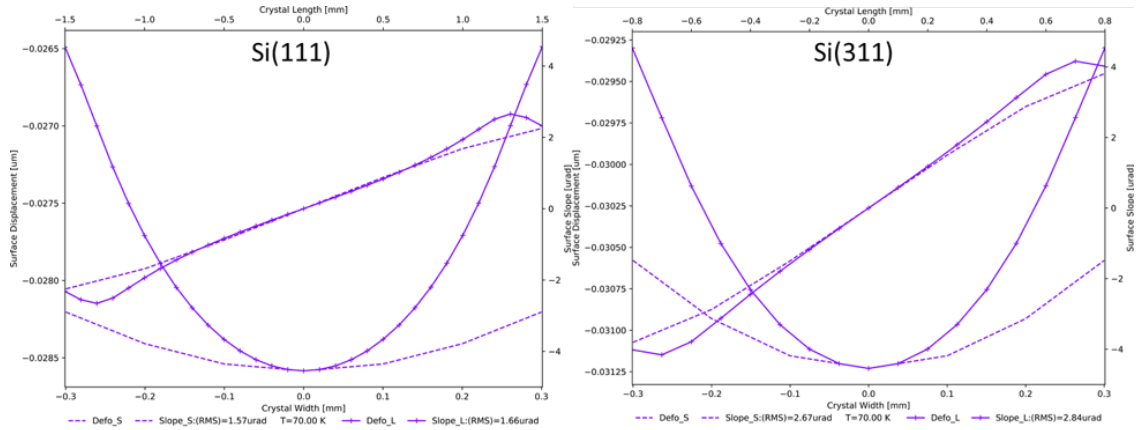

Figure 25: The 1st Crystal Surface Profile Thermal Performance.(Coolant temperature: 70 K; Thermal exchange co-efficiency: 0.005 W/mm2 / degree C)

2.10.4 Motion of optics

In recent years, a great deal of effort has been directed toward improving the angular stability of monochromators. There are now several examples of liquid nitrogen double crystal monochromators that have demonstrated a pointing stability below 100 nrad[44, 45].

2.10.5 Visualization

We will install beam visualization diagnostics after each major optical element in the beam path and near the downstream end of the experimental floor. These will be used to align the optical system, provide quality assurance checks, and for comparison to simulation. This latter activity is expected to be important, given the interplay between the optical elements in our scheme to provide variable coherence properties and focal spot size.

2.10.6 Feedback

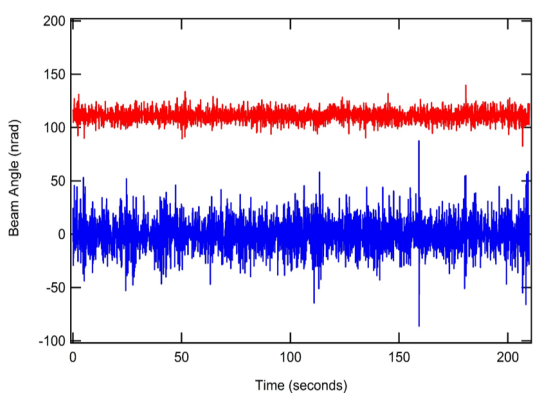

Figure 27: Recent results from the feedback stabilized beam position at HXN. Courtesy of Yong Chu.

Source-angle stability has been a study area at NSLS-II for the past several years. This activity has included the development of multiple feedback system, each using some different combination of the accelerator and beamline hardware, and a task force, comprised of photon and accelerator physicists, continues to meet regularly.

Feedback on electron beam trajectory normally acts on the input from electron beam position monitors. In the few sectors where x-ray beam position monitors are installed, the signal from both types of BPM is combined and this input results in more stable beam pointing.

X-ray photon BPMs are typically based on drain-currents measured through blades (The BPMs present in the beamline front ends are of this type.) or charge collection in a solid-state device, commonly comprised of diamond. Generally, this input signal results in a corrective motion of either the monochromator or one or more mirrors. We will first investigate the feasibility, including the expected response frequencies of our mirrors and monochromators

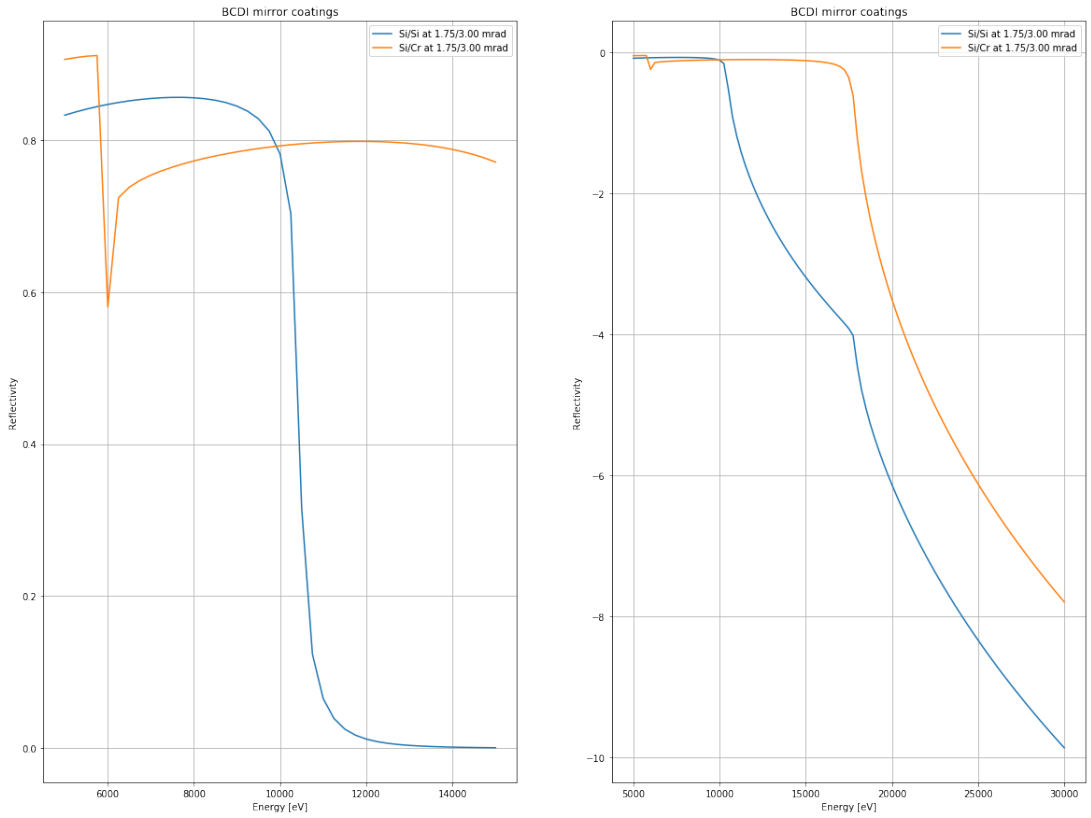

Figure 26: The total reflectivity of the proposed mirror system. The prefocusing mirrors have only a silicon surface, while the final focusing optics have silicon and chromium stripes. The reflectivity for the silicon stripes is shown in blue, while the chromium is shown in red.

as we finalize the designs. Given our dual-monochromator design, it might be advantageous to provide a feedback response with the mirrors, but additional study is needed to assess feasibility.

2.11 Exit window

In any coherence-preserving beamline, it is vital to choose a good exit window material and design. We propose to use a diamond window for the current project. Two considerations may require the alteration of this plan: (1) the window must be rather thin to allow operation at 5 keV, i.e., 50 microns or thinner; and (2) the displacement between the direct beam, coming past the final mirrors, and focused beam will be around 10 mm. If such a window cannot be acquired, we will consider an exit flange with multiple, smaller windows or a exit window made from Be. The final option is not preferred due to the potential contamination of the beam's phase by inclusions and voids within the Be.

3 Endstation Design

The proposed hutch is an irregular pentagon that is contained by a rectangle of 26 x 13 m and approximately 4 m tall. The concept is shown in detail below, during our discussion of the satellite building in Section 5. The remainder of this section describes the equipment within the hutch.

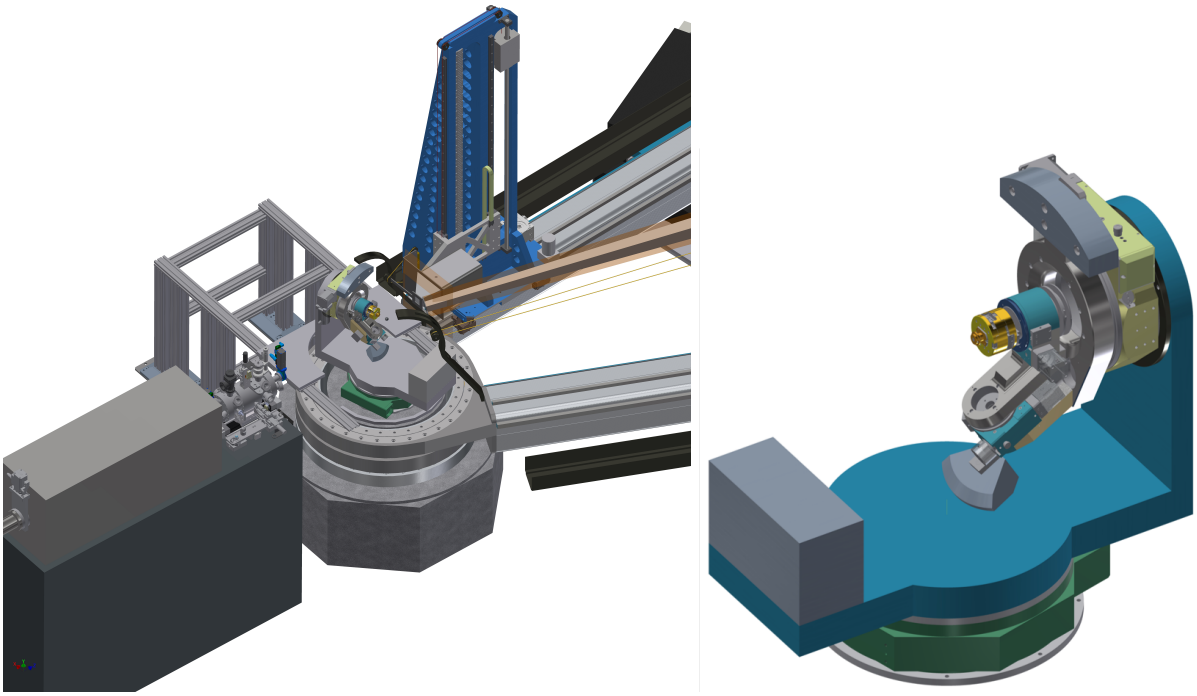

Figure 28: (left) A close-up view of the sample position in the endstation, note the large clearance provided. (right) An example of a kappa goniometer commercially available from Huber.

3.1 X-ray transport

We propose to preserve at least 500 mm of free space between the downstream end of the final mirror vessel and the sample location(See Fig. 28(left) for the concept.). Among the uses envisaged for this clear area is provisioning for:

- environmental cells to support in situ and operando science;
- "clean-up" slits, to condition the beam for demanding forward scattering CDI experiments;
- laser in-coupling and focusing optics, to support optical pump/x-ray probe experiments; and
- diagnostics, including for the beam position and intensity and, potentially, for monitoring the wavefront of the incident x-ray beam.

To support these, we will provide an optical-table or similar in the intervening space.

3.2 Sample positioning

3.2.1 Goniometer

We tentatively propose a kappa goniometer for orienting the sample. Our preference to the kappa geometry is driven solely by the desire to provide as flexible a diffraction geometry as possible. The Huber model 515 will permit a load of 2.5 kg, which combines the mass of the sample, its cell–if any–and the sample scanning stages. We propose to allocate 1 kg of this total load to the sample and its cell, reserving the remainder for standard scanning and positioning stages. An example of one such diffractometer is shown in Fig. 28(right). We do not believe that this geometry will accommodate all foreseeable sample geometries, for example, in situ growth experiments will likely require large vacuum vessels. To support these experiments, we will design-in the planned capability to remove the standard goniometer and replace it with a limited-range-of-motion alternative.

3.2.2 Scanning stages

In order to meet the demands of the science case for the instrument, we need both nano-positioning and centimeter-scale scanning ranges. We will engage the nanopositioning group at NSLS-II to develop a detailed design for this system. Similar systems have been constructed by combining individual commercial components. In the current case, we will aim for a positional accuracy better than 50 nm. This requirement is driven by the scanning-probe variation of the CDI techniques, e.g., ptychography. Here, the sample is scanned with step size much smaller than the size of the illuminating probe beam, here with stability of about 5% of the probe beam size.

3.3 Environmental requirements

The system comprised of the optics, sample, and detector spans a significant distance on the experimental floor: approximately 13 m. The highest requirement on the stability is that between the sample and the optical axis of the incident x-ray beam. Here, the short term stability requirements are motion below 50 nm, as discussed above, and the long term drift should be reduced to 10s of nm per hour. This relative stability should be maintained over the 2.6 m length of the sample-optics system. The stability requirement of the detector with respect to the sample is determined by the impact of the motion of the diffraction pattern on the detector. This motion is effectively a blurring of the diffraction pattern in the detector, which, from an algorithmic point of view, is similar to illuminating the sample with a partially transversely coherent x-ray beam. From literature, we know that the method is very sensitive to partially coherent illumination (In Whitehead et al. [14], an illumination with a coherence length tens of times as large as the standard requirement, was shown to have detrimental effects on the reconstruction.) This motion should be minimized to the extent possible and we judge that a reasonable criterion is a motion of 5% of a detector pixel. The smallest commercially available CDI-compatible detector has a pixel size is 55 microns. Our sample-to-detector pointing stability target is then 350 nrad from all sources. If we achieve a pointing stability of 100 nrad or better in the optical design, our requirement on the sample-to-detector positional stability is 2.7 microns. Achieving this goal will require significant design effort, good temperature stability, and a vibrationally quiet location.

We have taken measurements of the vibrational stability of the experimental floor inside the NSLS-II building and in the hutch of 3-ID, HXN. The measurements are acquired with a pair of seismometers, with an active frequency window from 1 to 800 Hz. Fig. 29(top) shows a typical plot of the vertical displacement of the experimental floor, integrated over the 2 to 100 Hz range, against time. The corresponding horizontal displacement is shown in Fig. 29(bottom). In both figures, the large spikes, which occur late at night or in the early morning, can be correlated with freight train activity south of the BNL site. The violet trace was collected near the boundary of the experimental floor and the bypass corridor surrounding it. The curves consistent show that the vertical displace is approximately 5 nm RMS greater near the edge of the experimental floor, where the detector would be located in our 60-m layout. Similar measurements were conducted in the HXN hutch. An example is shown in Fig. 30. Generally, the magnitude of the vibrational motion is of order 20% less in the HXN hutch; however, the data from the 12th of February in this figure show that it is possible to have a relative stability on the order of 10 nm RMS inside the HXN hutch when the surrounding human activity is restricted, the corresponding relative stability of the experimental floor is nearly twice as large. Activity on the experimental floor cannot be restricted in this way and we do seen such a low value on any standard working day in that data.

Our stability requirements are generally phrased as requirements on the relative motion of two or more components. Realizing absolute requirements on devices requires a good understanding of the transfer function, i.e., how vibration is transferred from the floor to the relevant location on the device. Our plans are not yet sufficiently advanced to provide this. We can, however, examine the response of two places inside the HXN hutch and on the experimental floor as a function of displacement. Fig. 31 summarizes the this from a 0 m displacement of the two seismometers up to 11 m. The HXN floor generally outperforms the experimental floor. Notice that this plot of relative displacement normalizes out the vibrational advantage of the HXN floor, in other words, the absolute displacement between two points on the HXN hutch floor are significantly lower than on the experimental floor. Given the high stability requirements of the method and the distance over which we must maintain this stability, **we have a clear preference for an outbuilding such as that constructed for HXN**.

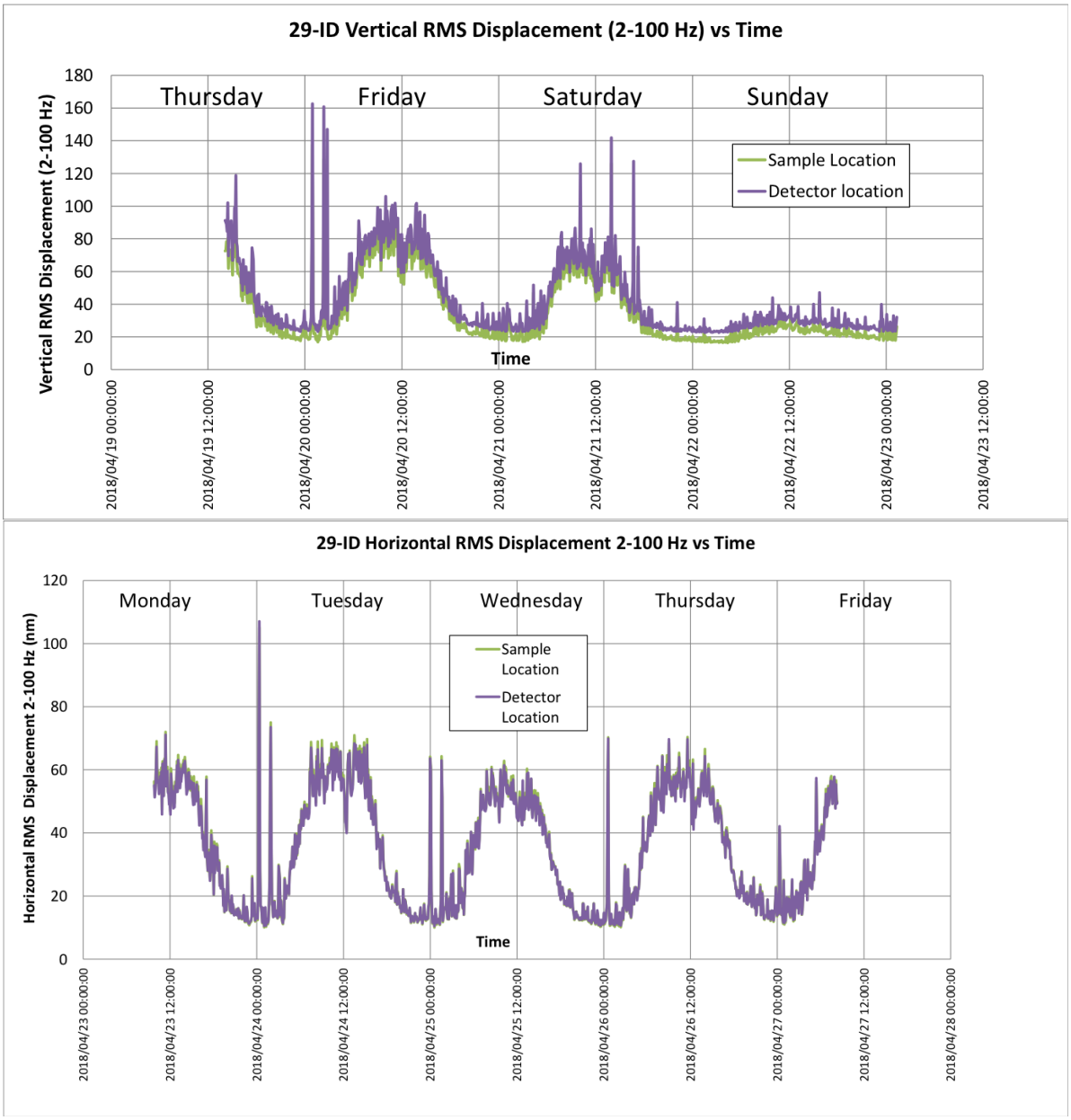

Figure 29: Plots of the RMS displacement of the experimental floor at sector 29-ID. The measurements were collected at two different locations on the 29-ID floor slot. The violet curve was near the tentative location of the detector in our scheme and shows high amplitude displacements. The green curve is derived from data collected near the tentative sample location. (Top) The measured vertical displacement. (Bottom) The measured horizontal displacement.

3.4 Detection

The method requires sampling according to the Shannon Theorem. Decreasing the coherence of the incident beam is, in the far-field under the normal CDI image formation assumption, a convolution between the fully coherent diffraction pattern and the propagated coherence function. The usual assumption is that the coherence function is featureless, i.e., a positive constant, over a domain of twice the sample's largest dimension. In this case, the convolution yields the fully coherent diffraction pattern. When transverse coherence is reduced, the diffraction pattern appears "blurred." As the illuminating coherence function

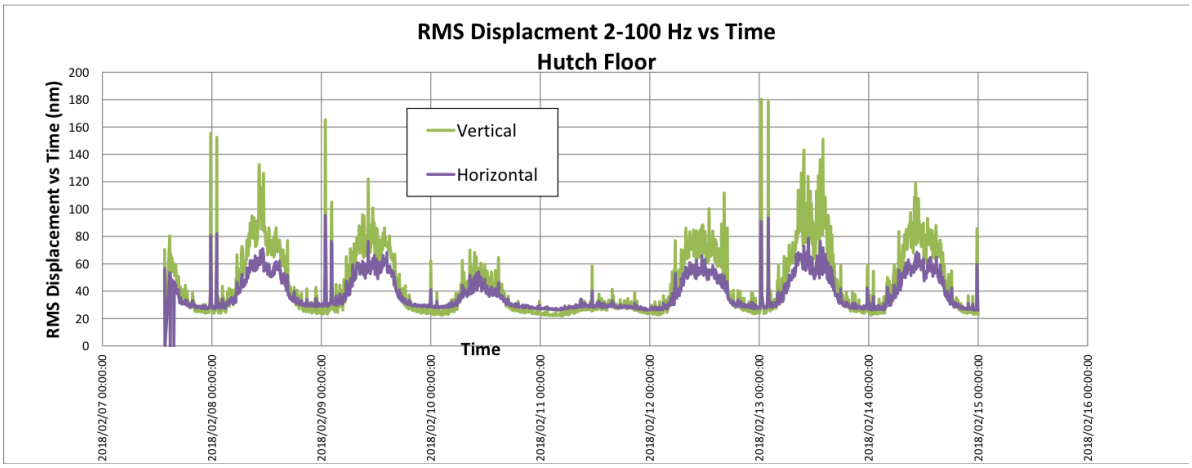

Figure 30: Plots of the RMS displacement of the hutch floor at HXN near the sample location. The green curve represents the vertical motion and the violet the horizontal. Note the difference between 2/12 and other weekdays, which illustrates the impact of human activity in the hutch.

becomes smaller than the object, the combined sample diffraction pattern becomes undersampled. In short, partially coherent CDI requires a higher sampling rate than its fully coherent counterpart. A conservative approach would be to increase the sampling rate by twice the ratio of the sample size to the coherence length.

The effect of imperfect longitudinal coherence has an angular dependence, whereby the blurring effect has an angular dependency, for forward-scattering CDI, the so-called polyCDI–polychromatic where a polychromatic illumination is introduced–this criterion has been derived and has been used in Table 5 to estimate the size of the object that the current beamline could be used to investigate without a translation scan of the sample. The entries in this table assume critical sampling of the diffraction pattern unless otherwise stated and, thus, present a best case scenario. An important consideration is that the sampling factors for the final two columns in the table are multiplicative, i.e., the largest sample that could imaged via CDI is a factor of 12 smaller than the original, critically sampled CDI criterion provides (This neglects the enhanced requirement on longitudinal coherence for Bragg CDI, as discussed above. The largest FCC, elemental metal crystal that could be imaged with a 1% bandpass DMM is likely to be smaller than 100 nm.).

In large part, the maximal use of partially coherent illumination in CDI has not been explored. Some development is certainly required, but the potential benefits are large: two decades of increased flux from decreased longitudinal coherence and one decade from decreased transverse coherence could allow CDI on a micron sized object simultaneous to Bragg CDI on a 50 nm crystal with an illuminating field of 10^14 photons. This would be an excellent basis for the very-high spatial resolution imaging of heterogeneous functional materials.

Below, we use the following equation to relate detector properties to the field of view and resolution of a final image produced by CDI. We define the following to represent the physical quantities relevant to the imaging process:

N the number of pixels in the detector;

d_1 the pixel size in real space;

d_2 the size of a pixel in the detector;

λ the wavelength of the radiation;

z the sample to detector distance.

The pixel size of the real-space, d_1, is related to the physical size of the detector, $Nd2$, by $d_1 = \lambda z/Nd_2$. Generally, the image resolution is defined by the extent of the diffraction pattern on the detector. In this formalism, the maximum size of the object under investigation, in 1D, is less than $d_1 N/2$. This requirement

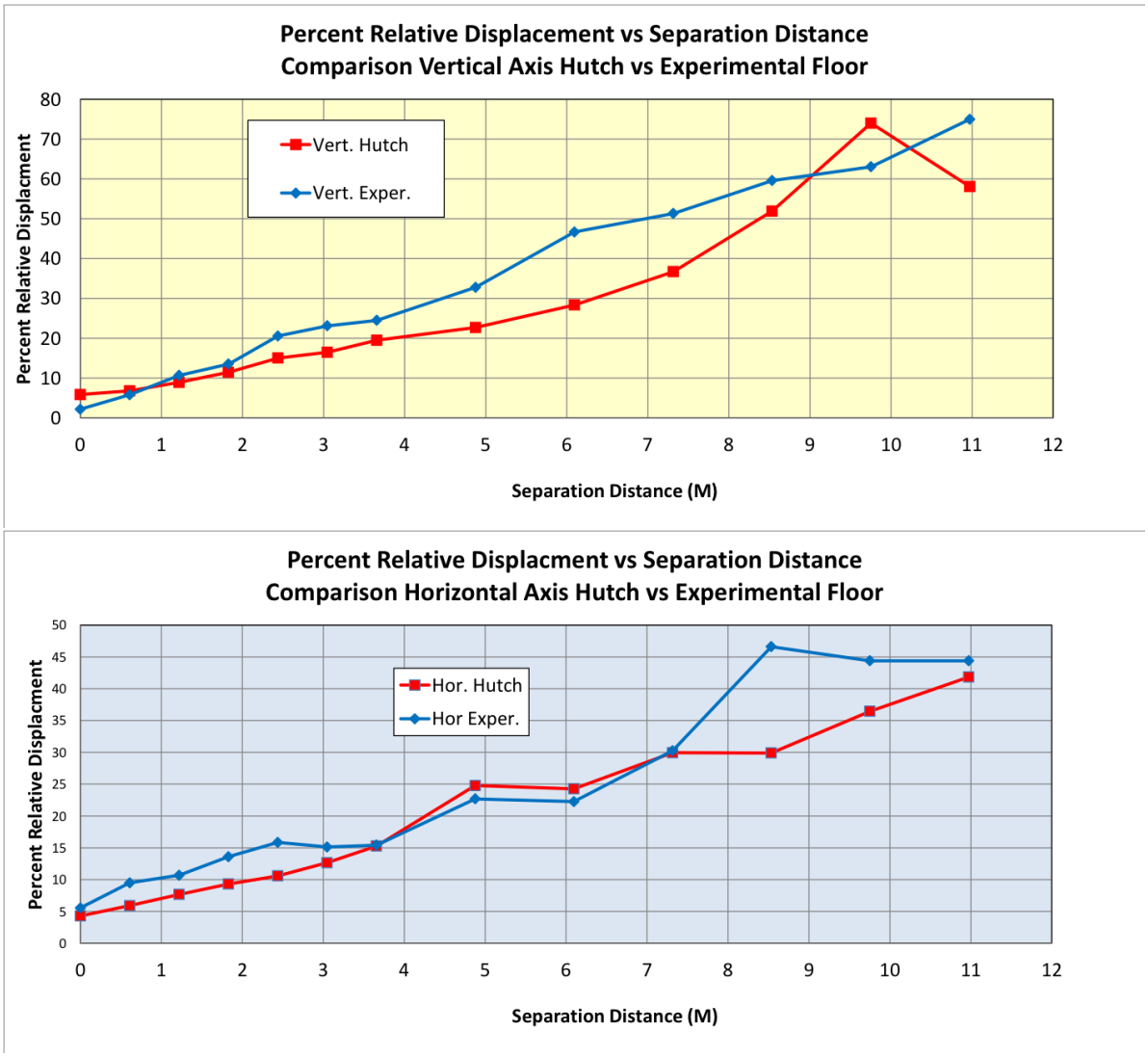

Figure 31: Plots of the percent relative displacement as a function of separation on the experimental floor at 29-ID, shown in blue, and inside the hutch at HXN, shown in red. (Top) The measured vertical displacement. (Bottom) The measured relative displacement in the horizontal. Note that this percent relative displacement is normalized by the absolute displacement, i.e., the advantage of the HXN floor is greater than is immediately obvious.

ensures appropriate sampling for a general object of size $N/2$, which, in turn, is required to assure the uniqueness, for all practical purposes, of a success reconstruction. Below, we will present a detection geometry informed by these considerations.

3.4.1 Detector technology

Since CDI requires the adequate sampling of a diffraction pattern, whose intensity spans many orders of magnitude, detectors that operate via direct photon detection are preferred. For the energy range discussed in this document, 5 to 15 keV, the quantum efficiency of silicon detectors is above 95%, so we propose the adoption of a silicon pixel array detector. Common devices include the Eiger–produced by Dectris–and the Medipix-derived products, such as the Excalibur. As multiple commercially available options are likely to exist on our procurement timeline, we will choose the detector based on an assessment, in order of importance, of its (1) single-photon detection capability; (2) dynamic range and read-out speed; and (3) pixel size. The

Energy [keV]	Detector pixel [micron]	Largest object size with critical sampling [micron]	Largest object size with typical sampling [micron]	Largest object size with polyCDI sampling [micron]	Largest object with half the transverse coherence [micron]
5	40	25	12	8.1	6.3
5	55	11	5.5	3.6	2.8
5	75	8.3	4.1	2.7	2.1
10	40	12	6	4	3
10	55	9	4.5	3	2.3
10	75	6.6	3.3	2.2	1.6
15	40	8.3	4.2	2.7	2.1
15	55	6	3	2	1.5
15	75	45	2.2	1.4	1.1

Table 5: A summary of the constraints on CDI experiments as a function of instrument photon energy, detector pixel size, and and sample-to-detector distance.

first is required for high-resolution CDI images. The second supports the imaging of material dynamics and might reduce stability requirements, depending on the period of the disturbance. The third, with the photon energy and the detector arm length, establishes the largest-sized object that can be investigated without a translational scan. The long detector arm and variability in the incident photon energy allows the de-emphasis of this final point and eases detection requirements. Table 5 is populated with nominal pixel sizes for these detectors: $d_2 = 75$ microns for the Eiger, $d_2 = 55$ microns for a Medipix-type camera, and $d_2 = 40$ microns as an estimate of the best-expected point-spread function for a detector with the necessary dynamic range.

In the case of a critically sampled diffraction pattern, i.e., the pixel pitch of the detector exactly matches the Nyquist sampling rate for the signal arising from the sample, the field of view of a CDI reconstruction is $d_1 N/2$. For example, we set a goal to to measure measure objects 10 microns or smaller at 10 nm or better resolution, which specifies a 2 000 x 2 000 pixel array detector.

3.4.2 Detector Positioning

Two considerations drive the positioning requirements on the detector motion system. First, as discussed above, the sample-to-detector distance is couple to the ultimate resolution of a CDI image by the radiation wavelength and the detector sampling period. Based on readily available detector technology, our photon energy range, and the scientific need to support the imaging of objects as large as 10 microns, we propose a maximum sample-to-detector distance of 8 m. This is the detector distance used in the calculations presented in Table 5. The minimum distance will be 0.5 m.

We seek to avoid the imposition of constraints on the sample geometry–because we recognize that the science cases supported by the instrument require flexibility in environmental cells and, potentially, positional orientation–by providing a generic detection geometry. We believe it feasible to elevate a detector to approximately 1.5 m above the beam axis. (A larger elevation would require an unusually tall x-ray hutch and the engineering required to position the detector accurately and stably becomes increasingly complex beyond this point.) The proposed elevation allows for a vertical scattering angle of 11 degrees at 8 m, and more than 70 degrees at 0.5 m. In the horizontal plane, we will allow the detector to move continuously between -5 and 120 degrees, with respect to the x-ray beam. This wide angular range is driven by a number of considerations. First, at 5 keV, it is not unusual for low-order reflections to have total scattering angles approaching 90 degrees. Second, the sensitivity to deformation in Bragg CDI increases with the order of the reflection under measurement, so the highest strain sensitivity is only available by accessing large scattering angles. Third, to maximize the feasibility of measuring multiple peaks from a single crystal, flexibility in the detection should be maximized. Finally, the ability to access near-backscattering reflections would be a unique capability.

As described in the introduction, we propose to support two independent area detectors with our detection scheme. As shown in Fig. 32, each detector will move independently along a predetermined arc centered on

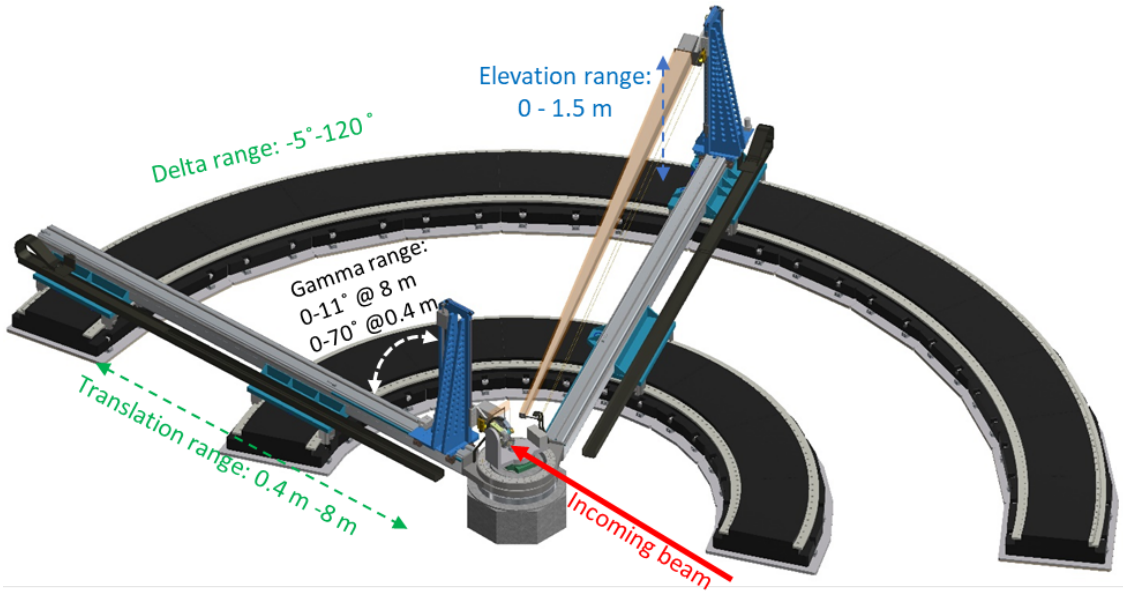

Figure 32: The detector motion system concept. Two detectors move independently along an arc with a continuous variable radius between 0.5 and 8 m. In the horizontal plane, scattering angles up to 120 degrees are possible. In the vertical, the maximum angle is 11 degrees at 8 m and 70 degrees at 0.5 m.

the sample location in the horizontal plane and elevated vertically. An additional tip axis will be provided to allow the detector to be perpendicular to the ray originating from the sample. He-filled flight paths, not shown, will prevent unnecessary attenuation of the diffraction signal.

3.5 Time-resolved provisioning

The beamline will be constructed with support for time-resolved measurements, although no specific apparatus is included in the scope. Timing hardware is proposed to consist of a fast-timing event receiver that receives signals directly, via fiber, from the NSLS-II event generator.

Similarly, although no laser system is included in the scope of the beamline project, we have included the construction of a room suitable for a laser system, utilities support for such a system, and safety infrastructure.

4 Controls Considerations

We will follow the best-practices established by previous beamline construction projects and the NSLS-II controls group. The highest risk task in this area is the control of our unusual two-detector geometry. We have engaged the NSLS-II data acquisition group to discuss the scope of work required to routinely use these for data collection and believe that this can be achieved.

5 Preliminary Comments on a Satellite Building

We propose to construct a satellite building to house the CDI beamline. HXN is only other beamline at NSLS-II with similar environmental–vibrational and thermal–requirements and we will modify that design to accommodate the larger footprint of the CDI endstation. A concept for this layout can be found in Fig. 33(Top) and (Middle). The total footprint of this concept is approximately the same as the HXN satellite building. (Please note the locations of hutch walls are not final in this version.) The concept for the design of the hutch itself will be similar to that of HXN, Fig. 33(bottom) shows a cross-sectional view of this

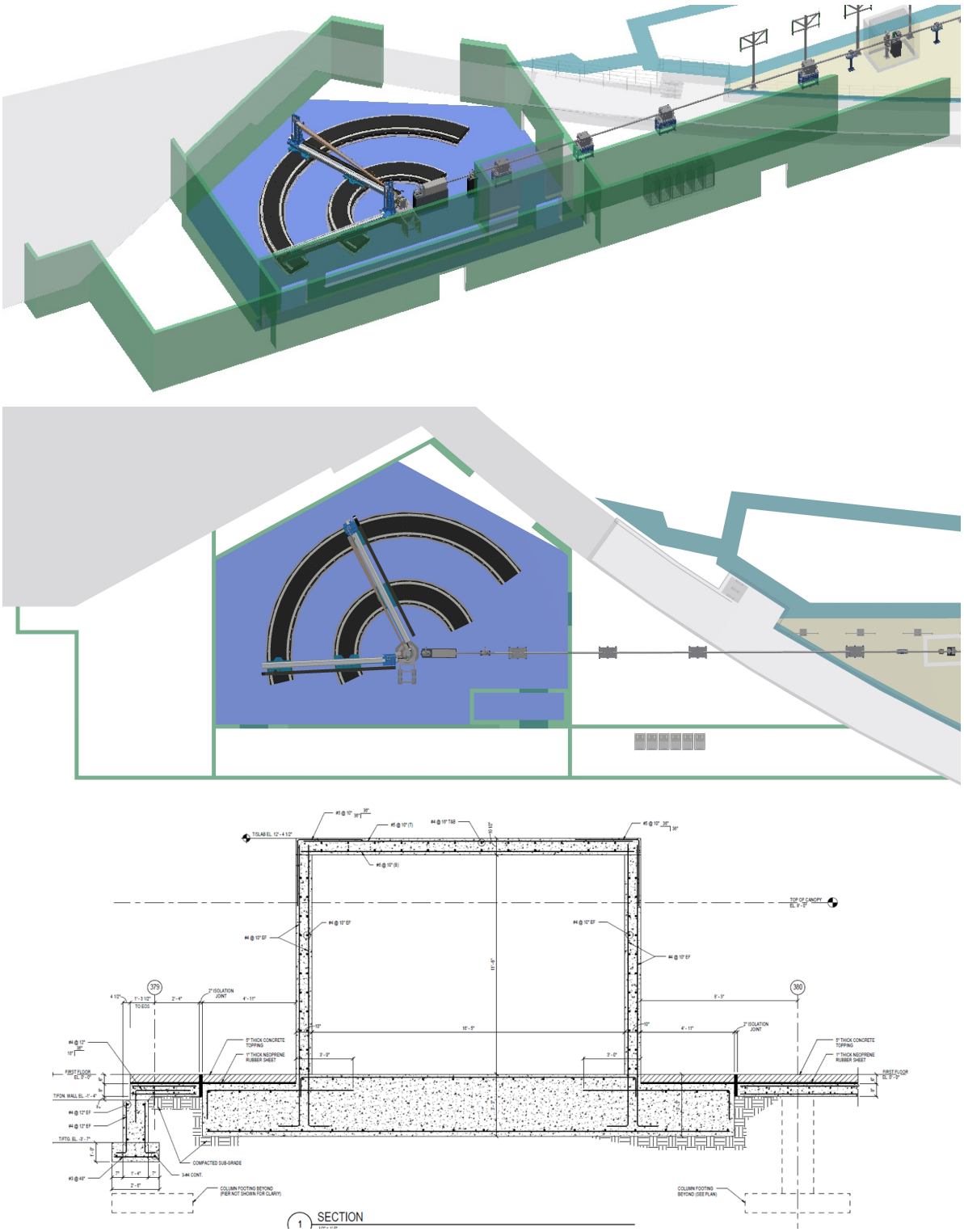

Figure 33: (Top) An isometric view of the proposed endstation and satellite building. (Middle) A top-down view of the same. Note the space reserved for a future laser enclosure in the lower right-hand corner. The total footprint is nearly identical to that of the HXN building. (Bottom) A cross section of the HXN hutch design that we propose to imitate. The floor thickness is 39” and the final wall thickness is 8”.

design. In short, all structural elements of the hutch will be composed of concrete. The floor thickness will be approximately 39", compared to the 15" thickness of the experimental floor. The wall and roof thickness of roughly 8" will add physical and thermal mass to the structure. The control room will be located near the endstation in the satellite building.

The satellite building will be accessible from the experimental floor, where a roll-up door will allow access for equipment, and through the neighboring LOB. A small area near the upstream, outboard corner of the hutch will be reserved for an optical laser, allowing its placement on the same slab as the rest of the endstation.

Preliminary inquires to the parties responsible for the specification and design of similar buildings, including those housing the endstations for the HXN and SIX beamlines and the HEX beamline project, have indicated that that our preliminary concept is feasible. Further study and the development of plans for a specific satellite structure will require further investment.

6 Safety

In addition to following standard NSLS-II safety procedures for containing radiation hazards and accessing x-ray hutches, the beamline design will provide appropriate emergency egress routes and the capability to handle samples and hazards associated with environmental cells safely. Care will be taken to ensure that the detector motion system can be operated safely. An integrated x-ray photon safety system and laser safety system will be needed; examples exist on operational NSLS-II beamlines.

Detailed safety information will be developed, in the future, for the preliminary design review.

References

[1] G. J. Williams, M. A. Pfeifer, I. A. Vartanyants, and I. K. Robinson. Three-Dimensional Imaging of Microstructure in Au Nanocrystals. *Physical Review Letters*, 90(17), April 2003. ISSN 0031-9007, 1079-7114. doi: 10.1103/PhysRevLett.90.175501. URL `https://link.aps.org/doi/10.1103/PhysRevLett.90.175501`.

[2] Mark A. Pfeifer, Garth J. Williams, Ivan A. Vartanyants, Ross Harder, and Ian K. Robinson. Three-dimensional mapping of a deformation field inside a nanocrystal. *Nature*, 442(7098):63–66, July 2006. ISSN 0028-0836, 1476-4687. doi: 10.1038/nature04867. URL `http://www.nature.com/doifinder/10.1038/nature04867`.

[3] Moyu Watari, Rachel A. McKendry, Manuel Voegtli, Gabriel Aeppli, Yeong-Ah Soh, Xiaowen Shi, Gang Xiong, Xiaojing Huang, Ross Harder, and Ian K. Robinson. Differential stress induced by thiol adsorption on facetted nanocrystals. *Nature Materials*, 10(11):862–866, September 2011. ISSN 1476-1122, 1476-4660. doi: 10.1038/nmat3124. URL `http://www.nature.com/doifinder/10.1038/nmat3124`.

[4] P. Godard, G. Carbone, M. Allain, F. Mastropietro, G. Chen, L. Capello, A. Diaz, T.H. Metzger, J. Stangl, and V. Chamard. Three-dimensional high-resolution quantitative microscopy of extended crystals. *Nature Communications*, 2:568, November 2011. ISSN 2041-1723. doi: 10.1038/ncomms1569. URL `http://www.nature.com/doifinder/10.1038/ncomms1569`.

[5] Marcus C. Newton, Steven J. Leake, Ross Harder, and Ian K. Robinson. Three-dimensional imaging of strain in a single ZnO nanorod. *Nature Materials*, 9(2):120–124, February 2010. ISSN 1476-1122, 1476-4660. doi: 10.1038/nmat2607. URL `http://www.nature.com/doifinder/10.1038/nmat2607`.

[6] Wonsuk Cha, Nak Cheon Jeong, Sanghoon Song, Hyun-jun Park, Tung Cao Thanh Pham, Ross Harder, Bobae Lim, Gang Xiong, Docheon Ahn, Ian McNulty, Jungho Kim, Kyung Byung Yoon, Ian K. Robinson, and Hyunjung Kim. Core-shell strain structure of zeolite microcrystals. *Nature Materials*, 12(8):729–734, July 2013. ISSN 1476-1122, 1476-4660. doi: 10.1038/nmat3698. URL `http://www.nature.com/doifinder/10.1038/nmat3698`.

[7] Wenge Yang, Xiaojing Huang, Ross Harder, Jesse N. Clark, Ian K. Robinson, and Ho-kwang Mao. Coherent diffraction imaging of nanoscale strain evolution in a single crystal under high pressure. *Nature Communications*, 4:1680, April 2013. ISSN 2041-1723. doi: 10.1038/ncomms2661. URL `http://www.nature.com/doifinder/10.1038/ncomms2661`.

[8] Jesse N. Clark, Johannes Ihli, Anna S. Schenk, Yi-Yeoun Kim, Alexander N. Kulak, James M. Campbell, Gareth Nisbet, Fiona C. Meldrum, and Ian K. Robinson. Three-dimensional imaging of dislocation propagation during crystal growth and dissolution. *Nature Materials*, 14(8):780–784, June 2015. ISSN 1476-1122, 1476-4660. doi: 10.1038/nmat4320. URL `http://www.nature.com/doifinder/10.1038/nmat4320`.

[9] S. O. Hruszkewycz, M. V. Holt, C. E. Murray, J. Bruley, J. Holt, A. Tripathi, O. G. Shpyrko, I. McNulty, M. J. Highland, and P. H. Fuoss. Quantitative Nanoscale Imaging of Lattice Distortions in Epitaxial Semiconductor Heterostructures Using Nanofocused X-ray Bragg Projection Ptychography. *Nano Letters*, 12(10):5148–5154, October 2012. ISSN 1530-6984, 1530-6992. doi: 10.1021/nl303201w. URL `http://pubs.acs.org/doi/10.1021/nl303201w`.

[10] D. Sayre. Some implications of a theorem due to Shannon. *Acta Crystallographica*, 5(6):843, 1952. ISSN 0365-110X. doi: 10.1107/S0365110X52002276. URL `http://scripts.iucr.org/cgi-bin/paper?S0365110X52002276`.

[11] Jianwei Miao, Pambos Charalambous, Janos Kirz, and David Sayre. Extending the methodology of X-ray crystallography to allow imaging of micrometre-sized non-crystalline specimens. *Nature*, 400(6742):342, 1999. doi: 10.1038/22498. URL `https://www.nature.com/articles/22498`.

[12] Advanced Photon Source. The APS upgrade, 2010. URL `https://www.aps.anl.gov/APS-Upgrade`.

[13] European Synchrotron Radiation Facility. The ESRF-EBS project, 2015. URL https://www.esrf.eu/about/upgrade.

[14] L. W. Whitehead, G. J. Williams, H. M. Quiney, D. J. Vine, R. A. Dilanian, S. Flewett, K. A. Nugent, A. G. Peele, E. Balaur, and I. McNulty. Diffractive Imaging Using Partially Coherent X Rays. *Physical Review Letters*, 103(24), December 2009. ISSN 0031-9007, 1079-7114. doi: 10.1103/PhysRevLett.103.243902. URL https://link.aps.org/doi/10.1103/PhysRevLett.103.243902.

[15] Brian Abbey, Lachlan W. Whitehead, Harry M. Quiney, David J. Vine, Guido A. Cadenazzi, Clare A. Henderson, Keith A. Nugent, Eugeniu Balaur, Corey T. Putkunz, Andrew G. Peele, G. J. Williams, and I. McNulty. Lensless imaging using broadband X-ray sources. *Nat Photon*, 5(7):420–424, July 2011. ISSN 1749-4885. doi: 10.1038/nphoton.2011.125. URL http://www.nature.com/nphoton/journal/v5/n7/full/nphoton.2011.125.html.

[16] M. Gailhanou, A. Loubens, J.-S. Micha, B. Charlet, A. A. Minkevich, R. Fortunier, and O. Thomas. Strain field in silicon on insulator lines using high resolution x-ray diffraction. *Applied Physics Letters*, 90(11), 2007. ISSN 0003-6951, 1077-3118. doi: 10.1063/1.2713335. URL http://aip.scitation.org/doi/10.1063/1.2713335.

[17] Magnus Heurlin, Tomas Stankevic, Simas Mickevicius, Sofie Yngman, David Lindgren, Anders Mikkelsen, Robert Feidenhans'l, Magnus T. Borgstrom, and Lars Samuelson. Structural Properties of Wurtzite InP-InGaAs Nanowire Core-Shell Heterostructures. *Nano Letters*, 15(4):2462–2467, April 2015. ISSN 1530-6984, 1530-6992. doi: 10.1021/nl5049127. URL http://pubs.acs.org/doi/10.1021/nl5049127.

[18] Meliha G. Rainville, Christa Wagenbach, Jeffrey G. Ulbrandt, Suresh Narayanan, Alec R. Sandy, Hua Zhou, Randall L. Headrick, and Karl F. Ludwig. Co-GISAXS technique for investigating surface growth dynamics. *Physical Review B*, 92(21), December 2015. ISSN 1098-0121, 1550-235X. doi: 10.1103/PhysRevB.92.214102. URL https://link.aps.org/doi/10.1103/PhysRevB.92.214102.

[19] Alexei Grigoriev, Rebecca Sichel, Ho Nyung Lee, Eric C. Landahl, Bernhard Adams, Eric M. Dufresne, and Paul G. Evans. Nonlinear Piezoelectricity in Epitaxial Ferroelectrics at High Electric Fields. *Physical Review Letters*, 100(2), January 2008. ISSN 0031-9007, 1079-7114. doi: 10.1103/PhysRevLett.100.027604. URL https://link.aps.org/doi/10.1103/PhysRevLett.100.027604.

[20] J. E. Parks. Less Costly Catalysts for Controlling Engine Emissions. *Science*, 327(5973):1584–1585, March 2010. ISSN 0036-8075, 1095-9203. doi: 10.1126/science.1187154. URL http://www.sciencemag.org/cgi/doi/10.1126/science.1187154.

[21] C. H. Kim, G. Qi, K. Dahlberg, and W. Li. Strontium-Doped Perovskites Rival Platinum Catalysts for Treating NOx in Simulated Diesel Exhaust. *Science*, 327(5973):1624–1627, March 2010. ISSN 0036-8075, 1095-9203. doi: 10.1126/science.1184087. URL http://www.sciencemag.org/cgi/doi/10.1126/science.1184087.

[22] Amit Banerjee, Daniel Bernoulli, Hongti Zhang, Muk-Fung Yuen, Jiabin Liu, Jichen Dong, Feng Ding, Jian Lu, Ming Dao, Wenjun Zhang, Yang Lu, and Subra Suresh. Ultralarge elastic deformation of nanoscale diamond. *Science*, 360(6386):300–302, April 2018. ISSN 0036-8075, 1095-9203. doi: 10.1126/science.aar4165. URL http://www.sciencemag.org/lookup/doi/10.1126/science.aar4165.

[23] Preeti Ovartchaiyapong, Kenneth W. Lee, Bryan A. Myers, and Ania C. Bleszynski Jayich. Dynamic strain-mediated coupling of a single diamond spin to a mechanical resonator. *Nature Communications*, 5(1), December 2014. ISSN 2041-1723. doi: 10.1038/ncomms5429. URL http://www.nature.com/articles/ncomms5429.

[24] Shufen Fan, Junnan Zhao, Jun Guo, Qingyu Yan, Jan Ma, and Huey Hoon Hng. p-type Bi0.4sb1.6te3 nanocomposites with enhanced figure of merit. *Applied Physics Letters*, 96(18):182104, May 2010. ISSN 0003-6951, 1077-3118. doi: 10.1063/1.3427427. URL http://aip.scitation.org/doi/10.1063/1.3427427.

[25] Takashi Kimura, Satoshi Matsuyama, Kazuto Yamauchi, and Yoshinori Nishino. Coherent x-ray zoom condenser lens for diffractive and scanning microscopy. *Optics Express*, 21(8):9267, April 2013. ISSN 1094-4087. doi: 10.1364/OE.21.009267. URL `https://www.osapublishing.org/oe/abstract.cfm?uri=oe-21-8-9267`.

[26] Oleg Chubar, Pascal Elleaume, and Joel Chavanne. A three-dimensional magnetostatics computer code for insertion devices. *Journal of Synchrotron Radiation*, 5(3):481–484, May 1998. ISSN 0909-0495. doi: 10.1107/S0909049597013502. URL `http://scripts.iucr.org/cgi-bin/paper?S0909049597013502`.

[27] O Chubar and P Elleaume. Accurate and Efficient Computation of Synchrotron Radiation in the Near Field Region. *Proc. of EPAC-98*, pages 1177–1179, 1998.

[28] Y. Ivanyushenkov, K. Harkay, M. Abliz, L. Boon, M. Borland, D. Capatina, J. Collins, G. Decker, R. Dejus, J. Dooling, C. Doose, L. Emery, J. Fuerst, J. Gagliano, Q. Hasse, M. Jaski, M. Kasa, S.-H. Kim, R. Kustom, J.-C. Lang, J. Liu, E. Moog, D. Robinson, V. Sajaev, K. Schroeder, N. Sereno, Y. Shiroyanagi, D. Skiadopoulos, M. Smith, X. Sun, E. Trakhtenberg, I. Vasserman, A. Vella, A. Xiao, J. Xu, A. Zholents, E. Gluskin, V. Lev, N. Mezentsev, V. Syrovatin, V. Tsukanov, A. Makarov, J. Pfotenhauer, and D. Potratz. Development and operating experience of a short-period superconducting undulator at the Advanced Photon Source. *Physical Review Special Topics - Accelerators and Beams*, 18(4), April 2015. ISSN 1098-4402. doi: 10.1103/PhysRevSTAB.18.040703. URL `https://link.aps.org/doi/10.1103/PhysRevSTAB.18.040703`.

[29] C. Benabderrahmane, M. Valleau, A. Ghaith, P. Berteaud, L. Chapuis, F. Marteau, F. Briquez, O. Marcouille, J.-L. Marlats, K. Tavakoli, A. Mary, D. Zerbib, A. Lestrade, M. Louvet, P. Brunelle, K. Medjoubi, C. Herbeaux, N. Bechu, P. Rommeluere, A. Somogyi, O. Chubar, C. Kitegi, and M.-E. Couprie. Development and operation of a Pr 2 Fe 14 B based cryogenic permanent magnet undulator for a high spatial resolution x-ray beam line. *Physical Review Accelerators and Beams*, 20(3), March 2017. ISSN 2469-9888. doi: 10.1103/PhysRevAccelBeams.20.033201. URL `https://link.aps.org/doi/10.1103/PhysRevAccelBeams.20.033201`.

[30] J Chavanne, M Hahn, R Kersevan, C Kitegi, C Penel, and F Revol. CONSTRUCTION OF A CRYOGENIC PERMANENT MAGNET UNDULATOR AT THE ESRF. *Proc. of EPAC-08*, pages 2243–2245, 2008.

[31] O Chubar, J Bengtsson, A Blednykh, C Kitegi, G Rakowsky, T Tanabe, and J Clarke. Segmented Adaptive-Gap In-Vacuum Undulators -Potential Solution for Beamlines Requiring High Hard X-Ray Flux and Brightness in Medium Energy Synchrotron Sources? *Journal of Physics: Conference Series*, 425(3):032005, March 2013. ISSN 1742-6588, 1742-6596. doi: 10.1088/1742-6596/425/3/032005. URL `http://stacks.iop.org/1742-6596/425/i=3/a=032005?key=crossref.174ce10719e0f7bfe2a9f684baf6dbcc`.

[32] P Ilinski. Optimization of NSLS-II Blade X-ray Beam Position Monitors: from Photoemission type to Diamond Detector. *Journal of Physics: Conference Series*, 425(4):042006, March 2013. ISSN 1742-6588, 1742-6596.

[33] Oleg Chubar, Lonny Berman, Yong S. Chu, Andrei Fluerasu, Steve Hulbert, Mourad Idir, Konstantine Kaznatcheev, David Shapiro, Qun Shen, and Jana Baltser. Development of partially-coherent wavefront propagation simulation methods for 3rd and 4th generation synchrotron radiation sources. page 814107, San Diego, California, USA, September 2011. doi: 10.1117/12.892812. URL `http://proceedings.spiedigitallibrary.org/proceeding.aspx?doi=10.1117/12.892812`.

[34] Oleg Chubar, Yong S. Chu, Konstantine Kaznatcheev, and Hanfei Yan. Application of partially coherent wavefront propagation calculations for design of coherence-preserving synchrotron radiation beamlines. *Nuclear Instruments and Methods in Physics Research Section A: Accelerators, Spectrometers, Detectors and Associated Equipment*, 649(1):118–122, September 2011. ISSN 01689002. doi: 10.1016/j.nima.2010.11.134. URL `http://linkinghub.elsevier.com/retrieve/pii/S0168900210026811`.

[35] Garth J. Williams, Oleg Chubar, Ian K. Robinson, Lonny Berman, and Yong S. Chu. Optical design and simulation of a new coherence beamline at NSLS-II. In Kawal Sawhney and Oleg Chubar, editors, *Advances in Computational Methods for X-Ray Optics IV*, page 14, San Diego, United States, August 2017. SPIE. ISBN 978-1-5106-1233-4 978-1-5106-1234-1. doi: 10.1117/12.2274387. URL https://www.spiedigitallibrary.org/conference-proceedings-of-spie/10388/2274387/Optical-design-and-simulation-of-a-new-coherence-beamline-at/10.1117/12.2274387.full.

[36] J.C.H. Spence, U. Weierstall, and M. Howells. Coherence and sampling requirements for diffractive imaging. *Ultramicroscopy*, 101(2-4):149–152, November 2004. ISSN 03043991. doi: 10.1016/j.ultramic.2004.05.005. URL http://linkinghub.elsevier.com/retrieve/pii/S0304399104000956.

[37] L. Mandel and E. Wolf. *Optical Coherence and Quantum Optics*. Cambridge University Press, 2008. ISBN 9780521417112. URL https://books.google.com/books?id=FeBix14iM70C.

[38] Tetsuya Ishikawa, Kenji Tamasaku, and Makina Yabashi. High-resolution X-ray monochromators. *Nuclear Instruments and Methods in Physics Research Section A: Accelerators, Spectrometers, Detectors and Associated Equipment*, 547(1):42–49, July 2005. ISSN 01689002. doi: 10.1016/j.nima.2005.05.010. URL http://linkinghub.elsevier.com/retrieve/pii/S016890020501096X.

[39] T. Graber. Efficiency of horizontal monochromators for APS-U beamlines. Technical report, Advanced Photon Source, Argonne National Laboratory. URL https://www.aps.anl.gov/files/APS-sync/lsnotes/files/APS_1708398.pdf.

[40] Lonny E. Berman, Zhijian Yin, Steven B. Dierker, Eric Dufresne, Simon G. J. Mochrie, Ophelia K. C. Tsui, Stephen K. Burley, Fong Shu, Xiaoling Xie, Malcolm S. Capel, and Robert M. Sweet. Performance of the double multilayer monochromator on the NSLS wiggler beam line X25. pages 71–79, Ithaca, New York (USA), 1997. doi: 10.1063/1.54629. URL http://aip.scitation.org/doi/abs/10.1063/1.54629.

[41] A. Rack, T. Weitkamp, M. Riotte, D. Grigoriev, T. Rack, L. Helfen, T. Baumbach, R. Dietsch, T. Holz, M. Kramer, F. Siewert, M. Meduna, P. Cloetens, and E. Ziegler. Comparative study of multilayers used in monochromators for synchrotron-based coherent hard X-ray imaging. *Journal of Synchrotron Radiation*, 17(4):496–510, July 2010. ISSN 0909-0495. doi: 10.1107/S0909049510011623. URL http://scripts.iucr.org/cgi-bin/paper?S0909049510011623.

[42] Christian Morawe, Jean-Christophe Peffen, Eric Ziegler, and Andreas K. Freund. High-resolution multilayer x-ray optics. pages 61–71, San Diego, CA, January 2001. doi: 10.1117/12.411658. URL http://proceedings.spiedigitallibrary.org/proceeding.aspx?articleid=920735.

[43] L Zhang, R Barrett, K Friedrich, P Glatzel, T Mairs, P Marion, G Monaco, C Morawe, and T Weng. Thermal distortion minimization by geometry optimization for water-cooled white beam mirror or multilayer optics. *Journal of Physics: Conference Series*, 425(5):052029, March 2013. ISSN 1742-6588, 1742-6596. doi: 10.1088/1742-6596/425/5/052029.

[44] Haruhiko Ohashi, Hiroshi Yamazaki, Hirokatsu Yumoto, Taito Osaka, Makina Yabashi, Shunji Goto, and Tetsuya Ishikawa. Stabilization of X-ray Beamline Optics towards Tens of Nanoradian Levels at SPring-8/SACLA. *Synchrotron Radiation News*, 31(5):33–37, September 2018. ISSN 0894-0886, 1931-7344. doi: 10.1080/08940886.2018.1506241. URL https://www.tandfonline.com/doi/full/10.1080/08940886.2018.1506241.

[45] Paw Kristiansen, Jan Horbach, Ralph Dohrmann, and Joachim Heuer. Vibration measurements of high-heat-load monochromators for DESY PETRA III extension. *Journal of Synchrotron Radiation*, 22(4):879–885, July 2015. ISSN 1600-5775. doi: 10.1107/S1600577515005664. URL http://scripts.iucr.org/cgi-bin/paper?S1600577515005664.